

1 Large-Scale Climate Modes Drive Low-Frequency Regional Arctic Sea Ice

2 Variability

3 Christopher Wyburn-Powell^a, Alexandra Jahn^a

⁴ *a Department of Atmospheric and Oceanic Sciences, and Institute of Arctic and Alpine Research,
5 University of Colorado Boulder, Boulder, Colorado*

This is the peer reviewed version of the following article: Wyburn-Powell, C., and A. Jahn, 2024: Large-Scale Climate Modes Drive Low-Frequency Regional Arctic Sea Ice Variability. *J. Climate*, 37, 4313–4333, <https://doi.org/10.1175/JCLI-D-23-0326.1>, which has been published in final form at <https://doi.org/10.1175/JCLI-D-23-0326.1>.

This article may be used for non-commercial purposes in accordance with Wiley Terms and Conditions for Use of Self-Archived Versions. This article may not be enhanced, enriched or otherwise transformed into a derivative work, without express permission from Wiley or by statutory rights under applicable legislation. Copyright notices must not be removed, obscured or modified. The article must be linked to Wiley's version of record on Wiley Online Library and any embedding, framing or otherwise making available the article or pages thereof by third parties from platforms, services and websites other than Wiley Online Library must be prohibited.

⁶ Corresponding author: C Wyburn-Powell, chwy8767@colorado.edu

7 ABSTRACT: Summer Arctic sea ice is declining rapidly but with superimposed variability on
8 multiple timescales that introduces large uncertainties into projections of future sea ice loss. To
9 better understand what drives at least part of this variability, we show how a simple linear model can
10 link dominant modes of climate variability to low-frequency regional Arctic sea ice concentration
11 (SIC) anomalies. Focusing on September, we find skillful projections from global climate models
12 (GCMs) from the Coupled Model Intercomparison Project Phase 6 (CMIP6) at lead times of 4-20
13 years, with up to 60% of observed low-frequency variability explained at a 5-year lead time. The
14 dominant driver of low-frequency SIC variability is the Interdecadal Pacific Oscillation (IPO)
15 which is positively correlated with SIC anomalies in all regions up to a lead time of 15 years, but
16 with large uncertainty between GCMs and internal variability realization. The Niño 3.4 Index and
17 Atlantic Multidecadal Oscillation have better agreement between GCMs of being positively and
18 negatively related, respectively, with low-frequency SIC anomalies for at least 10-year lead times.
19 The large variation between GCMs and between members within large ensembles indicate the
20 diverse simulation of teleconnections between the tropics and Arctic sea ice, and the dependence
21 on initial climate state. Further, the influence of the Niño 3.4 Index was found to be sensitive to
22 the background climate. Our results suggest that, based on the 2022 phases of dominant climate
23 variability modes, enhanced loss of sea ice area across the Arctic is likely during the next decade.

24 **SIGNIFICANCE STATEMENT:** The purpose of this study is to better understand the drivers of
25 low-frequency variability of Arctic sea ice. Teasing out the complicated relationships within the
26 climate system takes a large number of examples. Here we use 42 of the latest generation of global
27 climate models to construct a simple linear model based on dominant named climate features to
28 predict regional low-frequency sea ice anomalies at a lead time of 2-20 years. In 2022, these
29 modes of variability happen to be in the phases most conducive to low Arctic sea ice concentration
30 anomalies. Given the context of the longer-term trend of sea ice loss due to global warming, our
31 results suggest accelerated Arctic sea ice loss in the next decade.

32 **1. Introduction**

33 Over the past four decades, summer Arctic sea ice has rapidly declined and is projected to
34 continue to decline in the future (Wang and Overland 2012; Notz and Stroeve 2016; Sigmond
35 et al. 2018). However, large variability on multiple timescales is superimposed on this declining
36 trend, which can lead to 10-20 year periods of accelerated sea ice loss but also to a period of
37 over a decade of no sea ice loss (Kay et al. 2011; Swart et al. 2015). Hence, it is not unexpected
38 that no new record low September sea ice area has occurred since 2012 (Francis and Wu 2020),
39 in particular as September internal variability is currently elevated due to the decrease in the
40 thickness and mean sea ice state (Goosse et al. 2009; Eisenman 2010; Jahn 2018; Mioduszewski
41 et al. 2019). The shelf seas have been the focus of the observed decline as well as of the impact
42 of internal variability, with lower average sea ice concentration and thinner ice making the area a
43 hotspot of internal variability over the past few decades (Lindsay and Zhang 2006; England et al.
44 2019; VanAchter et al. 2020; Årthun et al. 2021). The shelf seas are also coincident with areas of
45 interest for shipping (Eguíluz et al. 2016; Melia et al. 2017), natural resource exploration (Petrick
46 et al. 2017), and ecological changes (Kovacs et al. 2011). However, the current characteristics
47 of variability are likely transitory as the shelf seas in the next few decades will become more
48 reliably ice-free throughout the summer (Barnhart et al. 2016; Crawford et al. 2021), ending
49 the dominant role of internal variability in projection uncertainty for this region (Bonan et al. 2021).

51 The internal variability of Arctic sea ice acts on multiple timescales and has therefore been
52 challenging to cleanly separate from the forced response (Stroeve et al. 2007; Kay et al. 2011; Swart
53 et al. 2015; Dörr et al. 2023). High-frequency drivers such as atmospheric temperature and wind
54 anomalies are generally considered dominant over lower-frequency drivers (Ding et al. 2019; Olon-
55 scheck et al. 2019; Roach and Blanchard-Wrigglesworth 2022), but separating the drivers is difficult
56 due to large spatial and temporal heterogeneity in variability (Onarheim et al. 2018). By defining
57 low-frequency variability as periods of at least 2 years, approximately one quarter of September
58 pan-Arctic internal variability can be accounted for by low-frequency variability in a sample of
59 global climate models (GCMs) (Wyburn-Powell et al. 2022). Although low-frequency variability
60 is only a small component of internal variability, it promises some longer term predictability, as
61 the influence of initial conditions and high-frequency drivers of variability decay rapidly beyond
62 the current season (Blanchard-Wrigglesworth et al. 2011; Bonan et al. 2019; Bushuk et al. 2019),
63 and have been shown to be useful to a maximum of two-year lead time (Day et al. 2014; Yeager
64 et al. 2015; Bushuk and Giannakis 2017; Holland et al. 2019; Gregory et al. 2021; Wang et al. 2021).

65

66 There is some prospect of summer Arctic sea ice predictability at lead times greater than 2
67 years due to ocean heat transports (Zhang and Wallace 2015; Docquier et al. 2021) and climate
68 modes of variability (Guemas et al. 2016). However, results so far seem to be model dependent
69 (Tietsche et al. 2014; Blanchard-Wrigglesworth and Bushuk 2019), and our current length of
70 observations is likely too short to verify such relationships (Bonan and Blanchard-Wrigglesworth
71 2020; Karami et al. 2023). Despite these challenges, extra-tropical modes of sea level pressure
72 variability have been suggested to directly affect Arctic sea ice variability, but so far only
73 with strong evidence on high-frequency timescales (Ukita et al. 2007; Serreze et al. 2007;
74 L'Heureux et al. 2008; Zhang et al. 2019; Liu et al. 2021). Tropical teleconnections have also
75 been identified as influencing Arctic sea ice loss, primarily associated with Pacific sea surface
76 temperatures (SSTs) (Hu et al. 2016; Li et al. 2018a; Screen and Deser 2019; Ding et al. 2019;
77 Kim et al. 2020; Clancy et al. 2021; Jeong et al. 2022b; Simon et al. 2022), but also with
78 Atlantic variability (Day et al. 2012; Miles et al. 2014; Meehl et al. 2018; Li et al. 2018b;
79 Karami et al. 2023). Rossby wave trains are the primary mechanism linking tropical Pacific SST
80 anomalies to the Arctic (Yuan et al. 2018). These Rossby waves propagate from the tropics to

81 the Arctic in the order of two weeks (Alexander et al. 2002), but can have seasonal Arctic sea
82 ice effects due to persistent positive geopotential height anomalies and associated subsidence and
83 diabatic warming leading to reduced sea ice cover (Baxter et al. 2019; Hofsteenge et al. 2022).
84 These insights into drivers of variability show promise, but skillful regional sea ice predictions
85 combining multiple modes of variability at lower-frequency timescales has so far been elusive.

86

87 Assessing drivers of low-frequency variability in the climate system is difficult to do without
88 large quantities of consistent data, such as that available from single model initial-condition large
89 ensembles (Deser et al. 2020; Milinski et al. 2020). This requirement for assessing drivers of
90 low-frequency Arctic sea ice variability stems from a multitude of drivers likely interacting on
91 heterogeneous spatial and temporal scales to cause this variability (Zhang et al. 2020). This has,
92 so far, lead to a lack of consensus of many of the drivers at time periods in excess of 2 years,
93 especially as GCMs and observations have been shown to represent these relationships differently.
94 We therefore leverage all available GCMs from the Coupled Model Intercomparison Project
95 Phase 6 (CMIP6) archive to investigate model consensus of these low-frequency relationships.
96 Additionally, we do not prescribe the nature of any of these relationships such as linearity and
97 independence, and perform a detailed regional analysis as well as assess multiple lead times.
98 To enable interpretation of these potentially complex relationships in the climate system we use
99 machine learning which has been used successfully before to explain patterns of surface climate
100 variability (e.g. Barnes et al. 2019; Labe and Barnes 2022). With this coherent approach to
101 determine the drivers of low-frequency Arctic sea ice variability on multiple timescales and
102 locations, we determine the modes of variability which are simulated to have the largest impact and
103 use the resulting model to make predictions of low frequency SIC variability over the next decade.

104

105

106 **2. Methods**

107 *a. Data sources*

108 In order to gather sufficient data of both climate modes of variability and associated sea
109 ice concentrations, we use 42 GCMs with historical CMIP6 forcing (O’neill et al. 2016).
110 These GCMs are those for which both monthly sea ice concentration is available and the
111 full suite of climate mode data has been processed using the Climate Variability Diagnostics
112 Package (CVPD) (Phillips et al. 2014). In total we use 609 realizations, from 42 GCMs and
113 23 modeling centers; a full list can be found in Table 1. In using the full suite of CMIP6
114 GCMs we can get a consensus of low-frequency drivers of Arctic sea ice variability, as
115 individual GCMs have biases in their simulation of teleconnections (Dalelane et al. 2023), but
116 some systematic biases pervasive across CMIP5 are improved in CMIP6 (Fasullo et al. 2020).

117

118 Alternatives to the historical simulations which could provide a similarly large quantity
119 of data include future scenarios or pre-industrial control simulations. However, as the
120 mean-state and variability of the Arctic sea ice (VanAchter et al. 2020; Árthun et al. 2021)
121 and some aspects of the rest of the climate system such as El Niño Southern Oscillation
122 (ENSO) (Brown et al. 2020) or AMOC (Weijer et al. 2020) differ from present conditions,
123 this approach would be less appropriate to analyze near-contemporaneous variability. Despite
124 differences in mean state, we do utilize pre-industrial control simulations to assess the va-
125 lidity of our detrending methodologies, but not make projections, as detailed in section 2d.

126

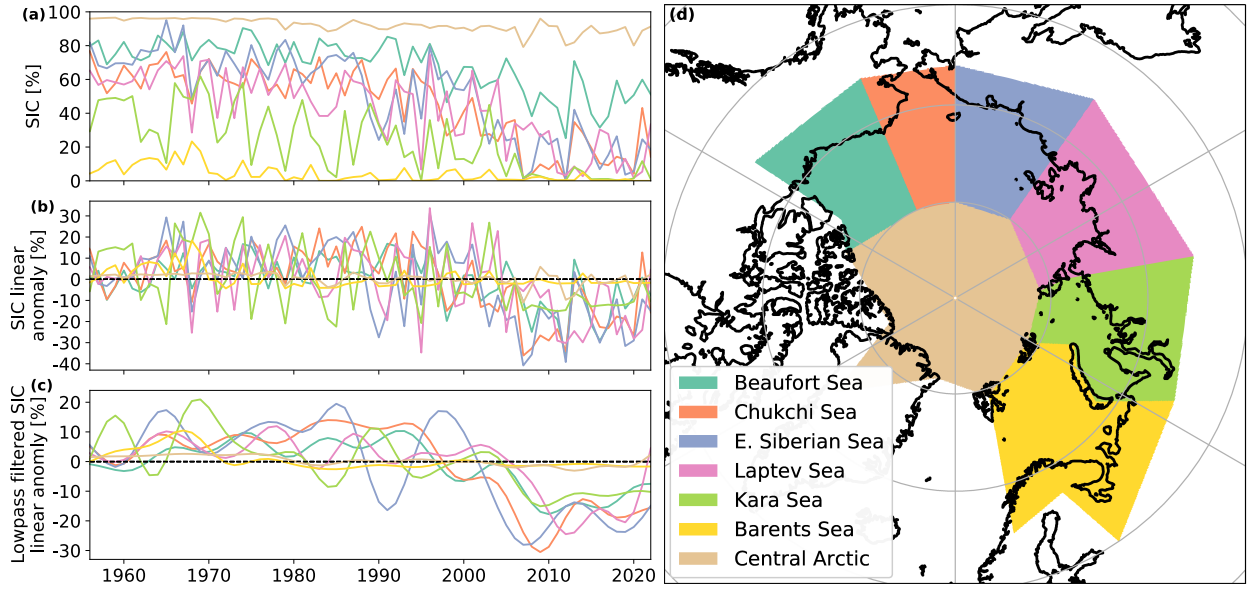
127 Within the historical period we use the 95-year time period 1920-2014 for sea ice concentration
128 (SIC), which we average over regions of the Arctic as defined by the National Snow and Ice Data
129 Center (NSIDC) Multisensor Analyzed Sea Ice Extent - Northern Hemisphere (Fetterer et al.
130 2010) (see Figure 1d). These seven regions cover the vast majority of the sea ice found during
131 the summer, although we do exclude the Canadian Arctic Archipelago due to complex coastal
132 zones which are typically poorly represented in GCMs (Long et al. 2021). We linearly detrend the
133 average SIC for each region and then apply a 2-year lowpass filter to exclude the high-frequency

¹³⁴ interannual variability and leave only the low-frequency anomalies (see Figure 1a-c). This low-
¹³⁵ pass filtered regional sea ice concentration data becomes the predictands in our regression analysis.

¹³⁶

TABLE 1. Global climate model output used in this analysis

Modeling Center	GCM Name	Members	Citation
CSIRO-ARCCSS	ACCESS-CM2	5	Dix et al. 2019
CSIRO	ACCESS-ESM1.5	40	Ziehn et al. 2019
BCC	BCC-CSM2-MR	3	Wu et al. 2018
BCC	BCC-ESM1	3	Zhang et al. 2018
CAMS	CAMS-CSM1.0	3	Rong 2019
NCAR	CESM2-FV2	3	Danabasoglu 2019a
NCAR	CESM2-LENS	50	Danabasoglu 2019b
NCAR	CESM2-WACCM	3	Danabasoglu 2019d
NCAR	CESM2-WACCM-FV2	3	Danabasoglu 2019c
THU	CIESM	3	Huang 2019
CMCC	CMCC-CM2-SR5	11	Lovato and Peano 2020
CNRM-CERFACS	CNRM-CM6-1	21	Voldoire 2018
CNRM-CERFACS	CNRM-ESM2-1	6	Seferian 2018
CCCma	CanESM5	65	Swart et al. 2019b
CCCma	CanESM5-CanOE	3	Swart et al. 2019a
E3SM-Project	E3SM1.0	4	Bader et al. 2019
EC-Earth-Consortium	EC-Earth3	23	EC-Earth-Consortium 2019a
EC-Earth-Consortium	EC-Earth3-CC	10	EC-Earth-Consortium 2021
EC-Earth-Consortium	EC-Earth3-Veg	7	EC-Earth-Consortium 2019b
EC-Earth-Consortium	EC-Earth3-Veg-LR	3	EC-Earth-Consortium 2020
FIO-QLNM	FIO-ESM2.0	3	Song et al. 2019
NOAA-GFDL	GFDL-ESM4	3	Krasting et al. 2018
NASA-GISS	GISS-E2-1-G	46	NASA Goddard Institute for Space Studies 2018
NASA-GISS	GISS-E2-1-H	25	NASA Goddard Institute for Space Studies 2019b
NASA-GISS	GISS-E2-2-G	11	NASA Goddard Institute for Space Studies 2019a
NASA-GISS	GISS-E2-2-H	5	NASA Goddard Institute for Space Studies 2019c
MOHC	HadGEM3-GC31-LL	5	Ridley et al. 2019a
MOHC	HadGEM3-GC31-MM	4	Ridley et al. 2019b
INM	INM-CM5-0	10	Volodin et al. 2019
IPSL	IPSL-CM6A-LR	32	Boucher et al. 2018
MIROC	MIROC-ES2H	3	Watanabe et al. 2021
MIROC	MIROC-ES2L	31	Hajima et al. 2019
MIROC	MIROC6	50	Tatebe and Watanabe 2018
HAMMOZ-Consortium	MPI-ESM1.2-HAM	3	Neubauer et al. 2019
MPI-M	MPI-ESM1.2-HR	10	Schupfner et al. 2019
MPI-M	MPI-ESM1.2-LR	30	Wieners et al. 2019
MRI	MRI-ESM2.0	12	Yukimoto et al. 2019
NUIST	NESM3	5	Cao and Wang 2019
NCC	NorCPM1	30	Bethke et al. 2019
NCC	NorESM2-LM	3	Seland et al. 2019
NCC	NorESM2-MM	3	Bentsen et al. 2019
MOHC	UKESM1.0-LL	16	Tang et al. 2019



137 **FIG. 1. Observed September sea ice concentrations for the seven Arctic regions used in this analysis.** The
 138 observational HadISST1 sea ice concentration data shown for (a) the regional average, (b) the linearly detrended
 139 version of (a), and (c) a 2-year lowpass filter applied on (b). What is shown in (c) is the data used in the analysis
 140 presented here. The outline of the different regions considered are shown in (d) and defined as for the National
 141 Snow and Ice Data Center (NSIDC) Multisensor Analyzed Sea Ice Extent - Northern Hemisphere (MASIE-NH)
 142 dataset (Fetterer et al. 2010).

143 We use nine variables from the CVDP to assess their influence on regional SIC anomalies in our
 144 regression analysis. Below we have included a brief description of these modes of variability, we
 145 have also included a citation of a relevant article using the same index. These climate modes of
 146 variability aim to capture different aspects of variability within the climate system, although some
 147 of these do overlap in spatial or temporal domains, and thus should not be considered independent.
 148 We obtain seasonal values for all variability modes which are then linearly detrended over the
 149 period 1920-2014 and standardized (if not already in such a format). As we lag the SIC data
 150 between 2 and 20 years from the CVDP data, only the latest 74 of the 95 year time period is used
 151 for a given lag time (1941-2014). When we present the linear effects of each mode of variability,
 152 we only use one seasonal value for the climate modes listed below (see 2b for selection of the
 153 season):

154

- 155 • AMO: Atlantic Multidecadal Oscillation, winter - DJF. The area-weighted SST anomalies in
156 the north Atlantic basin ($0\text{-}60^\circ\text{N}$, $80^\circ\text{W}\text{-}0^\circ\text{E}$), which is thought to have a period of approxi-
157 mately 60-80 years (Trenberth and Shea 2006).
- 158
- 159 • NAO: North Atlantic Oscillation, winter - DJF. The leading principal component of the
160 Atlantic ($20\text{-}80^\circ\text{N}$, $90^\circ\text{W}\text{-}40^\circ\text{E}$) seasonal average sea level pressure anomalies. Positive phase
161 indicates a relatively enhanced Azores high and deepened Icelandic low (Hurrell and Deser
162 2009). The NAO may have some small decadal predictability, such as from the AMO, but is
163 dominated by large interannual variability (Klavans et al. 2021).
- 164
- 165 • ATN: Atlantic Niño, spring - MAM. The area-averaged tropical Atlantic SST anomalies ($3^\circ\text{S}\text{-}$
166 3°N , $20^\circ\text{W}\text{-}0^\circ\text{E}$), with a similar periodicity to the Pacific El Niño/La Niña phases (Zebiak
167 1993).
- 168
- 169 • NINO34: Niño 3.4 Index, winter - DJF. 5-month running mean SST anomalies in the equato-
170 rial Pacific ($5^\circ\text{N}\text{-}5^\circ\text{S}$, $120^\circ\text{-}170^\circ\text{W}$). Values continuously in excess of $+0.4^\circ\text{C}$ for 6 months
171 indicate El Niño conditions, below -0.4°C indicates La Niña (Trenberth 1997). Such os-
172 cillations between positive and negative states occur approximately every 2-7 years in the
173 observational record.
- 174
- 175 • PDO: Pacific Decadal Oscillation, spring - MAM. The leading principal component of north
176 Pacific SST anomalies ($20\text{-}70^\circ\text{N}$, $110^\circ\text{E}\text{-}100^\circ\text{W}$). Positive phases are associated with positive
177 SST anomalies in the eastern Pacific and negative SST anomalies in the western and central
178 Pacific (Mantua et al. 1997). The PDO is thought to have a periodicity of approximately 50-70
179 years over the last 200 years (MacDonald and Case 2005).
- 180
- 181 • NPO: North Pacific Oscillation, spring - MAM. The second principal component of seasonal
sea level pressures over the north Pacific and North American continent ($20\text{-}85^\circ\text{N}$, $120^\circ\text{E}\text{-}$
 120°W) (Phillips et al. 2014). A positive phase is indicative of a deepened Aleutian low and
enhanced sea level pressure in the region of $20\text{-}40^\circ\text{N}$ as per Rogers (1981) who defined the
NPO based on geopotential height. A given phase usually persists on the order of a week.
- 182
- 183 • PNA: Pacific/North American Teleconnection, spring - MAM. The leading principal com-
184 ponent of seasonal sea level pressures over the north Pacific and North American continent

(20-85°N, 120°E-120°W) (Phillips et al. 2014). A positive phase is similar to the NPO with a deepened Aleutian low, but this mode of variability is more extensive, also including enhanced pressure over western Canada, see Leathers et al. (1991) who used geopotential height anomalies.

- IPO: Interdecadal Pacific Oscillation, spring - MAM. The leading principal component of 13-year lowpass filtered Pacific (40°S-60°N, 110°E-70°W) area-weighted SST anomalies. In its positive phase SST anomalies in the equatorial Pacific are positive with the western extra-tropical Pacific in both hemispheres experiencing cooler SST anomalies (Meehl et al. 2013). The period and symmetry of the IPO is thought to have varied considerably over time, but over the observational period it has been shown to change phase approximately every 20-30 years (Vance et al. 2022).

In addition to these modes of variability, we also include the summer (JJA) global average surface temperature (TAS), as motivated in section 2d.

Several additional modes of variability were also available from the CVDP but were not included in the final analysis. The modes investigated but not used are as follows: the Indian Ocean Dipole, the Atlantic Meridional Mode, the Southern Annular Mode, the North Pacific Index. All of these modes of variability had no measurable effect on the regression model. Furthermore, including the Northern Annular Mode led to over-fitting with the highly related NAO.

To compare model results to observations, we use SIC from the Hadley Centre Sea Ice and Sea Surface Temperature data set (HadISST1) (Rayner et al. 2003) for the period 1956-2022. We use the HadISST1 SIC record before the beginning of the satellite era in 1978 to enable longer analyses in our correlation analysis in section 3e. We start using the HadISST1 SIC data in 1956, as variability is degraded substantially before 1956 due to interpolations during winter (Rayner et al. 2003). However, when calculating linear trends for detrending, we use SIC data for 1920-2014 in order to be consistent with the GCMs. This is possible due to moderate confidence in the mean state for 1920-1955 despite the increased uncertainty in the interannual sea ice variability for that period. The HadISST1 data, similarly to the SIC in the

211 GCMs, is divided into regions, linearly detrended and interannual variability is removed with a
212 2-year lowpass filter. For observed climate variability data we also obtain these from the CVDP
213 where we use the HadISST1 dataset to calculate sea surface temperature-derived variables, the
214 NCEP-NCAR record for sea level pressures (Kalnay et al. 1996), and GISTEMP version 4 for
215 global surface temperatures (Lenssen et al. 2019). Similarly to the CVDP output variables for the
216 GCMs, we apply a linear detrending and standardization to the variables not already in this format.

217

218 *b. Machine Learning Methods*

219 To determine the relationship between the climate variability modes and the lagged effects on
220 regional Arctic SIC gain and loss, we use machine learning. Specifically we use neural networks
221 which excel at finding relationships within large data sets (e.g. Diffenbaugh and Barnes 2023). At
222 its simplest, the neural networks used here are multiple linear regression, but we can also account for
223 non-linear relationships and covariance by using more advanced neural network configurations. In
224 order to constrain the potentially complicated relationships between climate modes and subsequent
225 SIC changes, we require large quantities of data to train, validate and test our neural networks. We
226 therefore utilize three data sets as listed below, which fulfill different purposes:

227

- 12 LEs, individual CMIP6 GCM large ensembles of at least 20 members.

228

- MMLE 3+, all CMIP6 GCMs (42) with at least 3 members.

229

- MMLE 30+, all CMIP6 GCMs (8) with at least 30 members.

230 To determine the climate mode relationships with Arctic sea ice within an individual GCM we
231 require at least 20 members to provide sufficient data. This means we can train a neural network
232 separately on 12 of the 42 GCMs, referred to as LEs. To get a consensus across the 42 CMIP6
233 GCMs and weight them equally, we train a neural network on the 1st members of all 42 GCMs,
234 validate on the 2nd members and test on the 3rd members (the MMLE 3+). Finally, we also
235 train a neural network on the first 23 member of 8 GCMs with sufficiently large ensembles,
236 this allows us to see whether maximizing the available data increases predictive skill (MMLE 30+).

237

238 For all LEs, MMLE3+ and MMLE30+ we use a single seasonal time series from 8 climate
239 modes and TAS to predict lagged sea ice anomalies at one lead time, one region, and one sea ice
240 anomaly month at a time. Allowing any patterns between the lags, region or sea ice anomaly
241 months to be discovered rather than prescribed. The SIC anomalies are in % points for consistency
242 across regions. Hence, when comparing the influence of modes of variability in aggregate,
243 the % point change should be scaled by the variability of that region (as is done for Figure 8).
244 The use of % SIC deviation from the trend has identical meaning to using sea ice area and is
245 not sensitive to the mean state, other than the 0-100% bounds capping anomalies. The neural
246 networks have no knowledge of the initial sea ice state, but as the memory for the summer at lead
247 times in excess of 1 year is considered negligible (Giese et al. 2021), this omission is considered
248 unimportant at the timescales we consider. Further, including initial sea ice state as a predictand
249 would add complexity to our methods which would be difficult to constrain without additional data.

250

251 We utilize four configurations of machine learning model to test whether nonlinearities and
252 covariance between the climate modes is required to make skillful predictions of Arctic sea
253 ice anomalies. We achieve this by constructing four models listed below differing in their
254 linear or nonlinear relationships (activation functions) and whether they take into account
255 climate mode covariance (presence or absence of hidden layers). Model 1 has independent
256 linear relationships between the climate modes and sea ice anomalies, and hence is effectively
257 multiple linear regression. Model 2 is the same as model 1 but permits nonlinear relation-
258 ships. Model 3 uses only linear relationships but can take advantage of covariance between
259 climate modes, such as a positive phase of the IPO and a positive phase of the PDO having
260 a different combined effect than the individual effect of those modes. Model 4 is the most
261 complicated, allowing both nonlinear relationships and also covariance between the modes of
262 variability. For further details on the machine learning models see Supplementary section S1.

263

264 *c. Assessing Predictive Skill*

265 The threshold for our machine learning model to be useful at a given lag time is defined as when
266 its Pearson correlation coefficient for the validation data exceeds that obtained from persistence.
267 The persistence correlation coefficient in this instance is calculated from the 2-year lowpass filtered
268 regional SIC anomalies lagged between 2 and 20 years, the same lag times as used for our regression
269 analysis. When using the correlation coefficient, it is important to note that, especially at longer lag
270 times, there may be a high correlation between the linear model output and the validation data, but
271 this skill may be present with a smaller amplitude than for the validation data. Further, for regions
272 that are close to zero or 100% SIC, we are trying to predict very small variations in SIC. Hence
273 we could have poor predictability in these regions but still have small errors in absolute terms.

274

275 As we do not have sufficiently long periods of observations, we cannot train a separate machine
276 learning model on the observations. Instead, by pooling several regions and SIC anomaly months,
277 we calculate the proportion of positively and negatively correlated modes of variability with the
278 most extreme 10% of SIC positive and negative anomalies. This is not a way of verifying the GCM
279 predictive models per se, rather it shows the range of correlations present within a large ensemble
280 and allows observation to be placed alongside that range. Observations would be expected
281 to typically fall within the large ensemble distribution, but as we do not know how atypical
282 our one realization of reality is, we cannot ascribe meaning to differences from the ensemble
283 mean (Notz 2015). Similarly, when in section 3e we provide predictions of past and future
284 regional SIC anomalies, good agreement to observations does not explicitly validate our results.

285

286 *d. Sensitivities to time period and forcing*

287 We use a linear detrending for both the SIC and the CVDP variables over the period
288 1920-2014 as this is a simple process to understand and does not make specific assumptions
289 about the time period in question. This is not perfect as during that period the radiative
290 forcing as well as the observed and modeled sea ice decline were not entirely linear (see
291 Figure 1 from McBride et al. 2021 for global temperature). This means that some of the very

292 low-frequency variability of the forced response is incorporated into the anomalies of SIC and
293 CVDP variables, rather than being removed by detrending. Therefore, some predictability is
294 due to the shape of the forced response, primarily represented by our input variable of global
295 average surface temperature (TAS), and likely, to a small extent, the SST-derived variables
296 of NINO34, PDO, ATN, AMO, and the IPO. As the simple linear model used in our results
297 considers each variable independently, we can consider TAS similarly to a residual term in
298 the model which does not affect the conclusions we draw about other modes of variability.

299

300 To verify that our results from the period 1920-2014 are robust to different forcing conditions, we
301 compare results with a more linear forcing scenario for the historical period 1970-2014 and a con-
302 stant pre-industrial forcing scenario. For the 1970-2014 time period the global surface temperature
303 and sea ice area trends are both highly linear (Notz and Stroeve 2016; McBride et al. 2021). Conse-
304 quently, for 1970-2014 we find that the linear response to TAS in our models is far smaller than in
305 1920-2014 (see Figure S1, compared with Figure 4). The 1970-2014 time period, after accounting
306 for lags, only uses 24 years of data (compared with 74 for 1920-2014) and hence the linear response
307 is much more noisy than for 1920-2014. Therefore, although we get a broadly similar linear
308 responses for each climate mode, the low skill relative to persistence means we cannot use this
309 shorter time period, despite the more linear variables and more similar mean state to the present day.

310

311 Pre-industrial control runs (of which 35 GCMs are available to each provide 222 training years)
312 use constant 1850 radiative forcing and hence TAS trends are near zero over a 74-year time periods.
313 Despite the different mean state and variability, we still find very similar linear coefficients to the
314 1920-2014 time period, but with a smaller influence of TAS (see Figure S2 compared with Figure
315 4). However, the pre-industrial control results provide much smaller linear responses, likely due
316 to the 1850 mean-state exhibiting less variability than the 21st century, primarily due to thicker
317 Arctic sea ice (Kwok and Rothrock 2009). Despite the pre-industrial control climate being too
318 different to present day to make projections, the similar results to the 1920-2014 period implies that
319 the relationships are inherent to the climate system, not artifacts of the detrending methodology,
320 with the possible exception of NINO34 as discussed in section 4. We therefore use the 1920-2014

321 time period, despite the TAS and SIC nonlinearity, as it both captures similar SIC mean state and
322 variability to the present day, and enables the use of sufficient training data.

323 3. Results

324 a. A simple linear model captures drivers of low-frequency variability

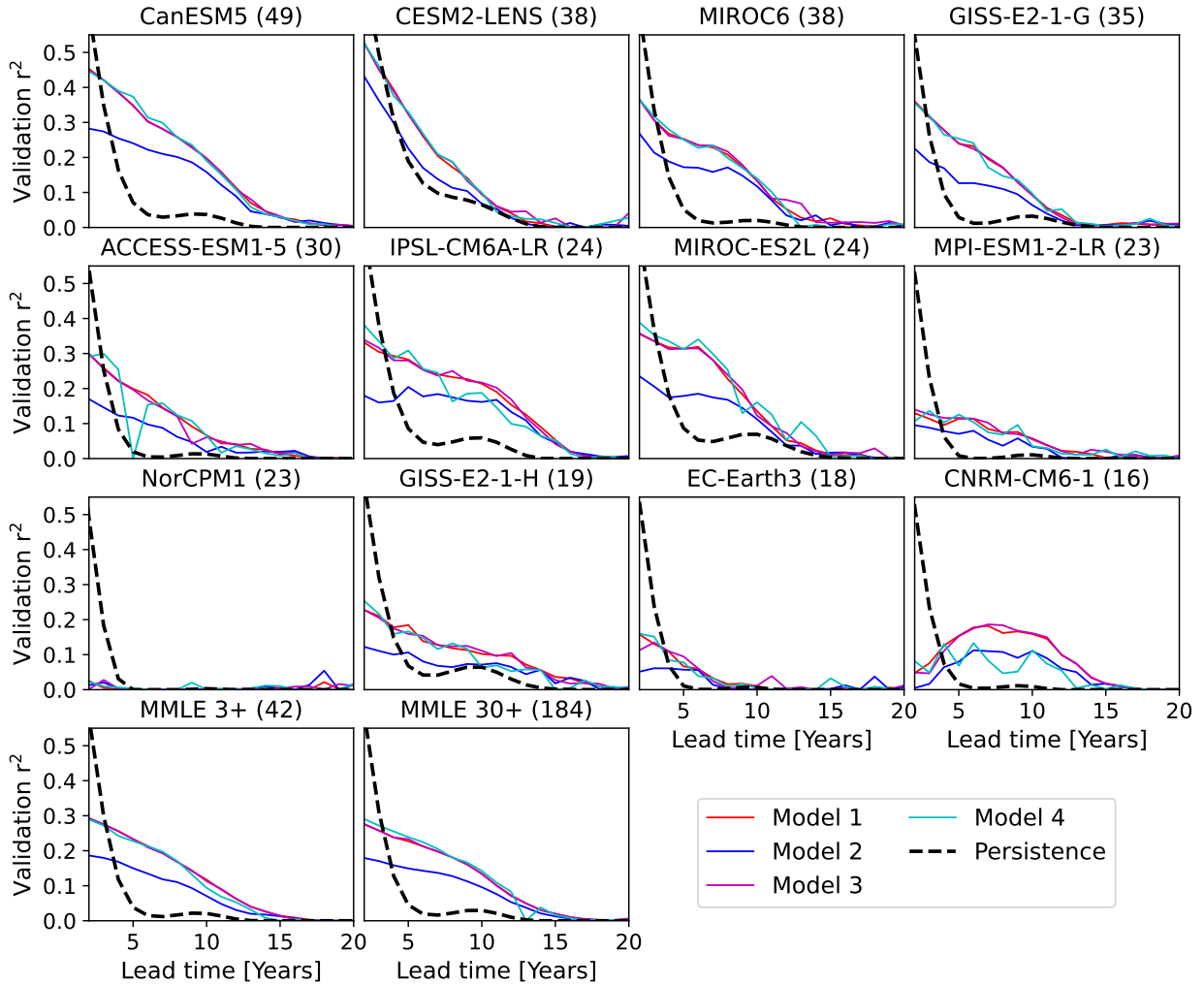
325 Predictions of regional low-frequency Arctic sea ice concentration anomalies can be produced
326 from climate modes of variability using a linear model, which are skillful when compared with
327 persistence. In general, we find that the simple linear variant of the machine learning models
328 (model 1) produces the highest predictive skill of the four models across GCMs, regions and
329 seasons. When validating our linear model we find it generally exceeds the skill from persistence
330 for lead times beyond approximately 4 years, but is dependent on the GCM (see Figure 2 for the
331 Chukchi Sea in September). The highest predictive skill is found at approximately a 5-year lead
332 time when the r^2 value of persistence has decayed close to zero while the r^2 value of the linear
333 model declines more slowly with lead time. This temporal pattern of persistence, as well as the su-
334 periority of the linear model, is found across regions and months with nonzero skill (see section 3b).

335

336 The simple linear model with no hidden layers (model 1) and the linear neural network
337 allowing climate mode covariance (model 3) are nearly identical in their performance across
338 different LEs and MMLEs (see Figure 2). The high performance of models 1 and 3 imply that
339 nonlinearities are not required to produce a skillful predictive model. The simple nonlinear
340 model 2 consistently performs poorly, with model 4 performing erratically for small training
341 data but can exceed the skill of other models for short lead-times and for the largest LEs and
342 MMLEs. As model 4 includes the effect of covariance of climate modes and nonlinearities,
343 this complex relationship between climate modes and sea ice anomalies is shown to only
344 provide a modest benefit to predictions. Subsequently, we therefore only utilize model 1, the
345 simple linear model, to clearly determine the independent linear effect of each climate mode of
346 variability. However, with additional data, the likely interdependent and nonlinear relationships

³⁴⁷ may be able to be detected robustly to allow greater generalization and produce better predictions.

348



349 **FIG. 2. The effect of machine learning model complexity on predictive skill.** Pearson correlation coefficients
 350 in the Chukchi Sea in September for the validation data for four machine learning models as shown for the 12
 351 LEs and 2 MMLE datasets. Model 1 refers to the simple linear model (red), model 2 to the simple nonlinear
 352 model (blue), and Model 3 and Model 4 to the fully-connected 9-3-3-1 neural network with linear (purple) and
 353 nonlinear (cyan) activation functions, respectively. The black dashed line indicates the average persistence for
 354 that lag time for the GCM or GCMs used. Where the model validation r^2 values exceed persistence the model
 355 has predictive skill. Numbers in parentheses indicate the number of ensemble members used in training.

356 *b. Hotspots of low-frequency variability predictive skill*

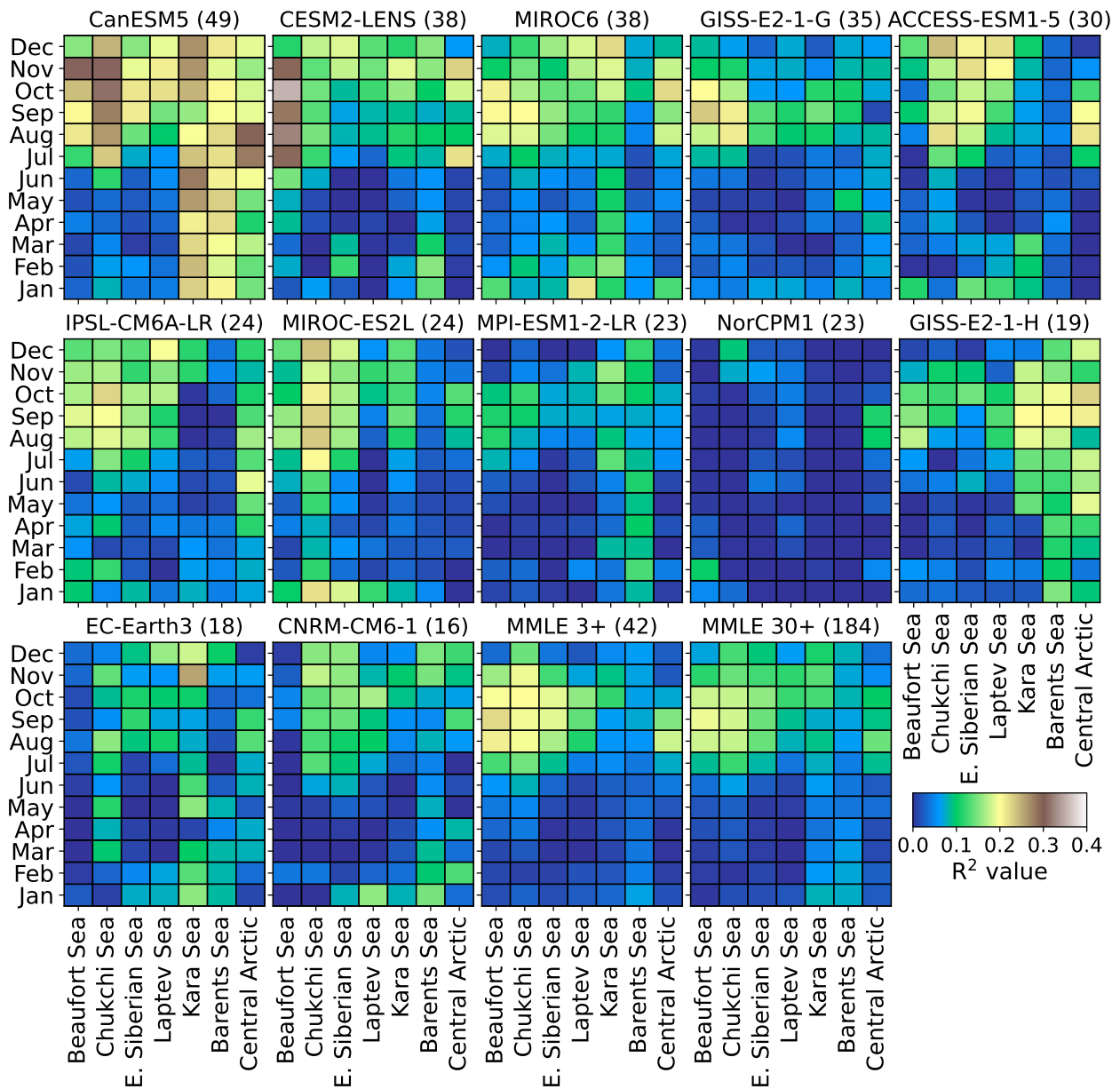
357 The summer and autumn marginal seas are generally able to produce the highest skill at
358 a 5-year lead time, however the predictive skill varies considerably between GCM. Based
359 on the MMLE 3+, which takes into account the full suite of CMIP6 GCMs with at least
360 3 ensemble members, the pattern of highest predictability is found in the Beaufort Sea in
361 September, with decaying skill for regions further from the Pacific and for months more
362 distant from September (Figure 3). The MMLE 3+ model is unable to produce high pre-
363 dictive skill in the Barents Sea for any season likely due to frequently near zero SIC, and
364 the Kara sea appears to have distinct peaks of predictive skill in July and late autumn.

365

366

367 For models using individual GCMs, the temporal and regional patterns of predictive skill
368 are often noisy for neighboring regions and months, unlike the clearer MMLE models. The
369 relatively high predictive skill values of the LEs typically exceed that of the MMLE 3+ for the
370 best regions, but with less coherence between regions and months. Selecting the LE with the
371 highest skill for a region and month may be appropriate, but each LE's specific spatial and
372 temporal limitations should be taken into account. The MMLE 3+ has lower predictive skill
373 than the best LEs, but is influenced by all 42 CMIP6 GCMs. Therefore, the relatively higher
374 predictive skill in the MMLE 3+ should be seen as less sensitive to individual GCM biases as
375 it is representative of the general agreement between all GCMs. Some LEs such as CanESM5
376 and ACCESS-ESM1-5 exhibit unusual patterns of high predictability in the Kara and Chukchi
377 Seas in the winter. Other LEs such as CESM2-LENS, GISS-E2-1-H and MIROC-ES2L have
378 particular regions which are far more predictable than others. For example, the CESM2-LENS
379 simulates high persistence for the Chukchi Sea but not for the Beaufort Sea (see Figure S4
380 for 5-year persistence, and section 3f for a CESM2 bias discussion) which causes the large
381 disparity in predictive skill between these two regions. As September is of particular interest
382 as the typical minimum annual pan-Arctic sea ice cover, and relatively high validation r^2 values
383 occur across regions for September in the MMLE 3+, this is our focus in subsequent analyses.

384



385 **FIG. 3. 5-year lagged predictive skill for multiple global climate models and the CMIP6 multi-model**
 386 **ensembles.** Pearson correlation coefficients are shown for the validation data minus persistence at a 5-year lag
 387 time between the input climate modes and sea ice concentration anomalies. Persistence is removed to indicate the
 388 regions and months for each LE or MMLE where predictive skill is high, rather than where explained variability
 389 is high. Numbers in parentheses indicate the total number of ensemble members used for training.

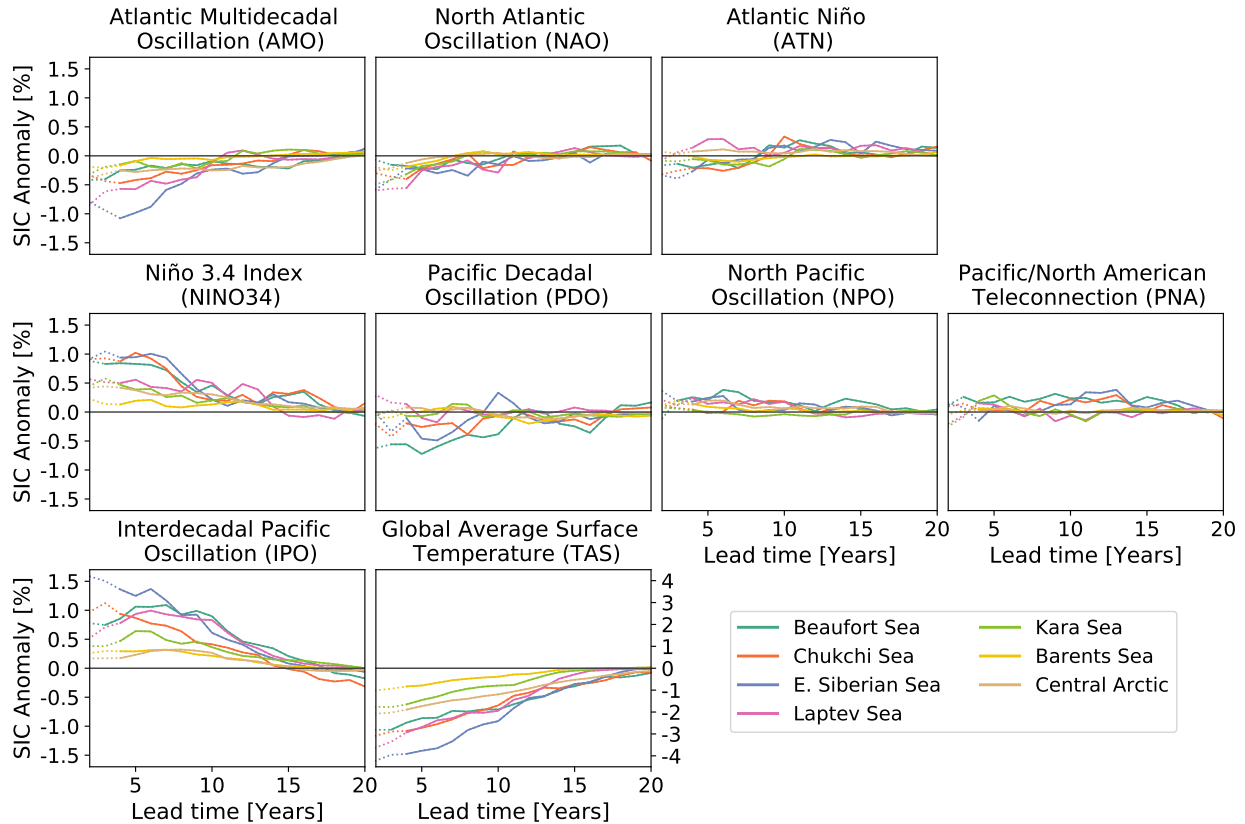
390 *c. Linear drivers of regional sea ice anomalies*

391 Using a linear model trained on 42 CMIP6 GCMs (the MMLE 3+ model), we can establish
392 the consensus across GCMs for the independent effect of each mode of variability on regional
393 September SIC anomalies. The lead times where the MMLE 3+ model has no predictive skill is
394 before a 4-year lead time for all regions except the Central Arctic where it is not until a 5-year
395 lag time that the validation r^2 exceeds persistence (see the dotted lines in Figure 4). The most
396 important mode of variability is the IPO, which is strongly positively correlated with the SIC
397 in all regions, especially in the East Siberian and Beaufort Seas (Figure 4). The IPO decays in
398 influence over time, reaching near zero influence on SIC at approximately a 15-year lead time.
399 The global average surface temperature (TAS) also has a very large coefficients, but as this is
400 not a mode of variability and is considered to integrate modes of variability not represented (see
401 section 2d for a more detailed explanation), we do not discuss in detail the influence of TAS further.

402

403 Aside from the large influence of the IPO, the Niño 3.4 index (NINO34) and the Atlantic
404 Multidecadal Oscillation (AMO) both display a very consistent sign of influence which decays with
405 time. The NINO34 and AMO both have smaller influences than the dominant IPO (approximately
406 one third and one quarter, respectively) for a given one standard deviation anomaly in each mode
407 of variability. Like the IPO and TAS, the influence of the AMO and NINO34 decays relatively
408 monotonically with time. As the skill of persistence also declines nearly monotonically, and the
409 IPO, TAS, NINO34 and AMO all display low-frequency variability, this increases confidence in the
410 validity of these relationships found in the MMLE 3+. The low-frequency oscillations of the other
411 sea surface temperature-derived indices of the Pacific Decadal Oscillation (PDO), and to a lesser
412 extent the Atlantic Niño (ATN), implies the potential for longer-term predictability as with the IPO,
413 TAS, NINO34 and AMO. However the influence of these modes is small at most time periods and
414 does not display a monotonic decline with time. This suggests these two modes are not highly im-
415 portant in driving low-frequency Arctic sea ice variability, but consistency or lack thereof between
416 LEs (see section 3d) may clarify whether the relationships in the MMLE 3+ are small and inde-
417 pendently consistent in magnitude between GCMs, or small due to disagreement between GCMs.

418



419 **FIG. 4. Linear drivers of September regional sea ice concentration anomalies.** Linear response of a +1
 420 standard deviation anomaly of each of the 8 climate modes and global average surface temperature on sea ice
 421 concentration anomalies in each of the seven Arctic regions. Positive SIC anomaly values indicate a positive SIC
 422 anomaly results from the +1 standard deviation anomaly in the climate mode of variability. Solid lines indicate
 423 that the validation r^2 value exceeds persistence for a given region and lead time, dashed lines indicate where there
 424 is no predictive skill beyond persistence. Non-zero predictive skill occurs for 4- to 20- year lead times for all
 425 regions except for the Beaufort Sea which has some predictive skill for a wider range of 3- to 20-year lead times.

426 The modes of variability based on sea level pressure patterns are generally a small influence
427 on low-frequency variability of Arctic sea ice. The Pacific/North American Teleconnec-
428 tion (PNA) and North Pacific Oscillation (NPO) do have some coherent regional effects
429 but the switch in sign of influence over time may be indicative of the expectation of a
430 change in the mode itself rather than the effect of the initial sign of the mode. Further, the
431 NPO and PNA are influenced by longer-lived modes of variability in the Pacific (Furtado
432 et al.), potentially meaning these modes are not independent. The North Atlantic Oscilla-
433 tion (NAO) is less erratic than the NPO and PNA with a general negative effect on SIC
434 anomalies but is very small in magnitude and is shown to affect SIC anomalies minimally.

435

436 *d. Low-frequency driver representation across global climate models*

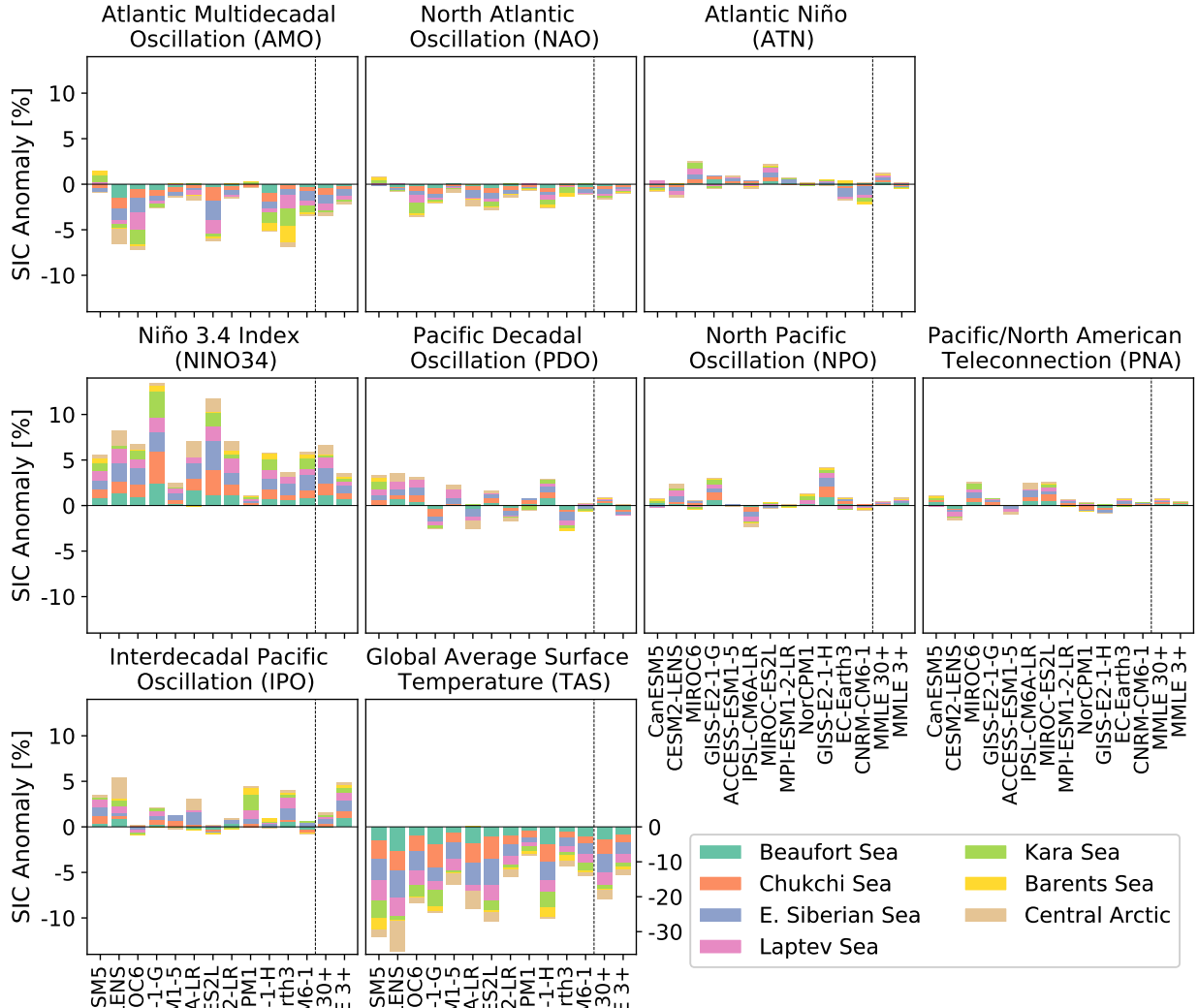
437 Comparing the independent results from 12 LEs aids our interpretation of the linear drivers of
438 SIC anomalies captured in the MMLE 3+. We do this by comparing the datasets for both the
439 medium-term for lead times of 4-9 years (Figure 5). Although the LE analysis only includes 12
440 of the 42 GCMs that went into the MMLE 3+ linear model, we can get a sense of the consistency
441 between the CMIP6-suite of GCMs. This informs our interpretation of the two dominant modes of
442 variability, namely the IPO and NINO34 with the LEs varying considerably for both modes of vari-
443 ability during both periods. Although the influence of the IPO and NINO34 are seen to gradually
444 decrease over time for the MMLE 3+, the individual LEs show large magnitudes of influence on
445 SIC for both time periods and the sign is inconsistent between LEs. We find little consensus across
446 GCMs on the sign of influence of the IPO across the 12 LEs. However, when we include these
447 same 12 GCMs and 30 others in the MMLE 3+, a more positive signal emerges. This suggests
448 either the additional 30 GCMs used in the MMLE 3+ have stronger positive linear relationships,
449 and/or that by chance the first members used in the MMLE 3+ have a disproportionately strong
450 positive relationship compared to the many members used for training in the LEs for a given GCM.

451

452 For the NINO34 there appears more consistency across the full CMIP6-suite of models with simi-
453 larities between the collection of 12 LEs and both MMLEs. This again highlights the importance of

454 taking a multi-model approach for the detection of low-frequency variability as two GCMs selected
455 at random may produce vastly different results. Further, although we use large ensembles, the
456 teleconnections between the tropics and Arctic may vary considerably between realization within
457 a large ensemble. Without pooling multiple GCMs and members we may not be able to capture
458 the full possible range of tropical-Arctic linkages which could be present over a 74-year time period.

459



460 **FIG. 5. The linear effect on regional SIC for 12 large ensembles and the two multi-model large ensembles.**

461 Linear response in September sea ice concentration for a +1 standard deviation anomaly of each climate mode,
 462 as in Figure 4, but averaged over two distinct lead times. Bars are the linear response averaged over 4 to 9-year
 463 lead times. Agreement within the CMIP6-suite of GCMs is high where bars are similar in magnitude and sign.
 464 Note the different y-axis scale for the global average surface temperature.

465 The AMO has reasonably good agreement between the LEs with almost all indicating
466 negative influence on regional SIC in the medium-term. The PDO in the MMLE 3+ has
467 near zero influence, across all 12 LEs we can see that none indicate the PDO as being
468 particularly influential, with disagreement in sign reducing the overall effect for the MMLE
469 3+. For the other modes of variability we find that almost all of the LEs coefficients
470 are small in magnitude and without overwhelming agreement on sign. This allows us to
471 interpret the MMLE 3+ near zero coefficients as being representative of both the lack of
472 consensus across CMIP6 GCMs and no strong relationships being found in any of the LEs.

473

474 The average magnitude of influence across all modes of variability differs considerably between
475 individual LEs. For example CESM2-LENS often produces the largest magnitudes for a given
476 mode and NorCPM1 the smallest. Such systematic differences may occur due to differences in
477 the mean state and magnitude of variability by GCM. This may well be the case considering
478 the SIC anomaly is recorded in percentage points and CEMS2-LENS has a low biased summer
479 mean-state (DuVivier et al. 2020) and consequently large variability. Conversely, NorCPM1 has
480 been noted as having a high biased sea ice thickness (Bethke et al. 2021), which may explain
481 why NorCPM1 is an outlier for small low-frequency SIC variability. Again, this indicates
482 care must be taken to understand the effect of limitations to the results from individual LEs.
483 Although many of the CMIP6-suite GCMs are related (Knutti et al. 2013), and their biases may
484 not average out, taking the results from the MMLE 3+ can reduce the risk of extreme outliers.

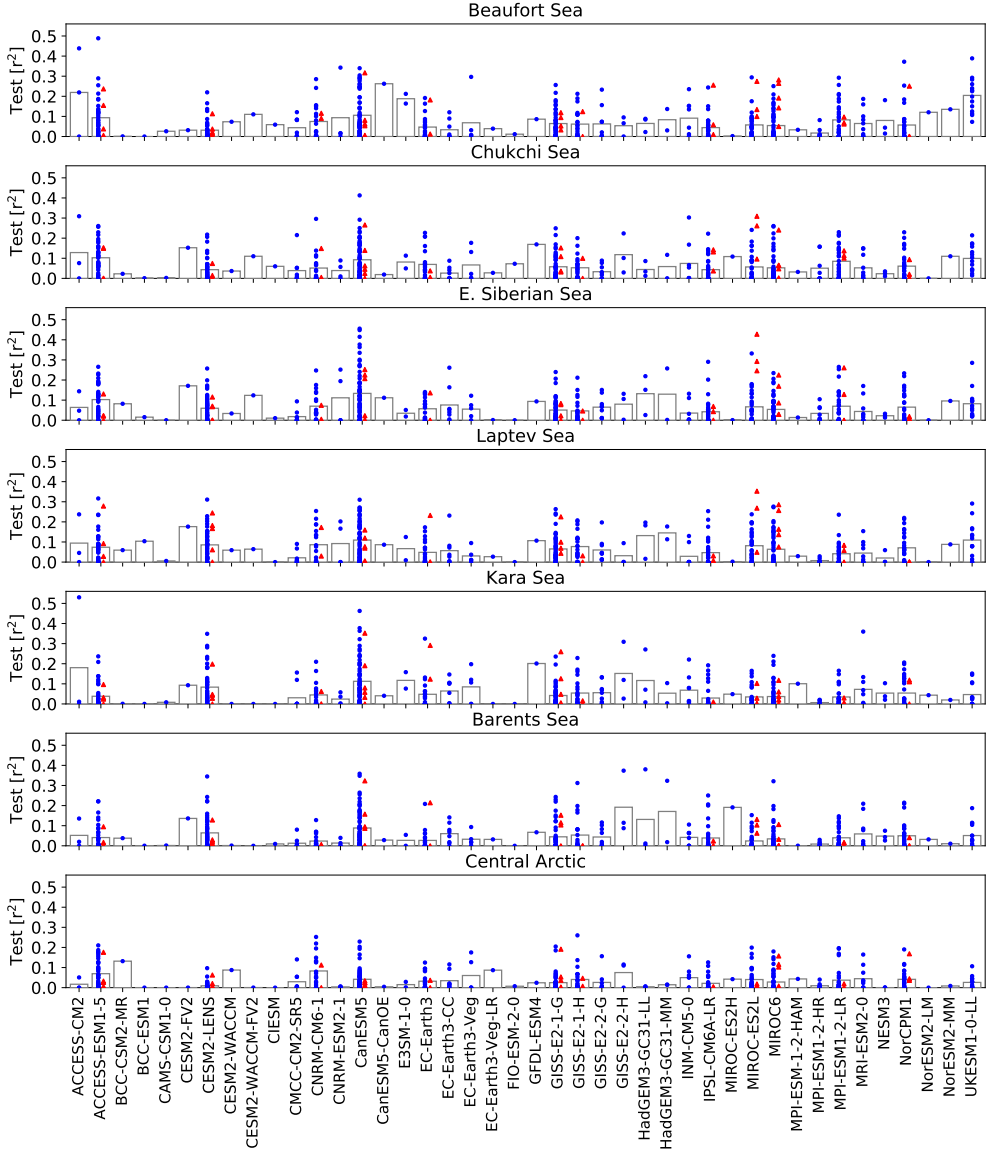
485

486 When testing our MMLE 3+ model on unseen members from the 42 GCMs, we find large vari-
487 ation between GCMs and ensemble members (see Figure 6). This limits our ability to determine
488 which GCMs are most like the CMIP6 consensus if they have small ensemble sizes which cannot
489 populate the full range of potential values (Notz 2015). Observational comparison with a similar
490 time period will therefore be also difficult as observations could be expected, due to internal
491 variability, to fall somewhere between 0 and $0.5 r^2$ if internal variability in the actual climate sys-
492 tem behaves similarly to the the range of ensemble members in a large ensemble such as CanESM5.

493

494 Despite the ensemble member disagreement, the MMLE 3+ model appears to be well generalized
495 to multiple GCMs as the test r^2 values appear very similar if a linear model is trained on all 42
496 GCMs as for the MMLE 3+ (blue circles in Figure 6) or only on other members from the same
497 GCM as for the LE (red triangles). CESM2-LENS has a wide distribution of test r^2 values between
498 ensemble members, with larger variations between the micro-perturbations (atmospheric state),
499 than between ensemble members with different ocean states (macro-perturbations) (see Figure
500 S3), as also found for pan- Arctic sea ice volume variability (Kay et al. 2022). This indicates that
501 for a 74-year time period, the specific manifestation of the relationships between climate variability
502 modes and regional Arctic SIC anomalies can be highly dependent on the initial climate state.

503

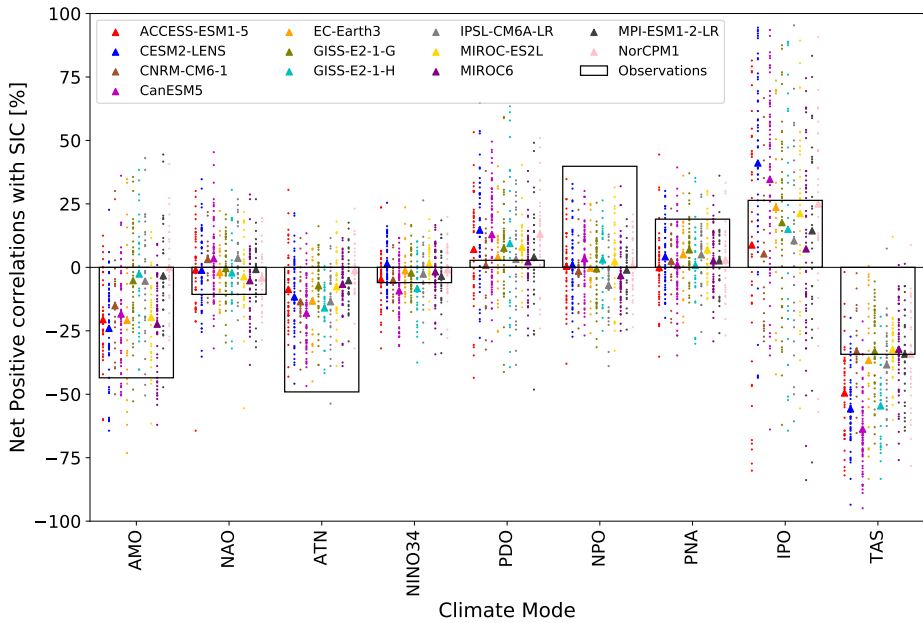


504 **FIG. 6. September r^2 values for the test ensemble members from either the multi-model large ensemble**
 505 **(3+, blue) or the 12 single GCM large ensembles (red).** The performance of the test members (third and later
 506 ensemble members) for the 42 GCMs included in the MMLE 3+ model are shown as blue circles, ensemble
 507 mean values are indicated by gray bars. The red triangles indicate the performance of the test members for the
 508 individually trained linear models for each of the 12 LEs, where 10% of the LE members were reserved for
 509 testing against the linear model trained and validated on the first 75% and 15% of members from each GCM.
 510 Where the red triangles and blue circles for a given GCM have a similar distribution, the MMLE 3+ is equally
 511 good at capturing the relationships between climate modes and SIC as the LE, indicating the MMLE 3+ is well
 512 generalized. The r^2 values are for a 5-year lead time minus persistence.

513 *e. Observational comparisons*

514 Correlations between the climate modes and extreme SIC anomalies show observations
515 broadly fall within what is simulated for the LEs, but validation is difficult due to the large
516 differences between realizations. In order to directly compare observations with ensemble
517 members, we compute the correlation between the 6 most extreme regional SIC anomaly years
518 in the period 1956-2022 and correlate whether each mode of variability was in a positive or
519 negative phase. To make a more representative sample, we pool the seven regions (except
520 the Barents Sea where summer variability is near zero), averaged over a 4- to 9-year lead
521 time. However, the correlations should not be seen as comparable to the linear model as the
522 correlations are binary, unlike the abilities of the linear model to apply lower weights to less
523 important climate modes. Observations fall within the ensemble spread for all GCMs for all
524 modes of variability except for the AMO which falls outside of only the NorCPM1, and the
525 ATN and NPO which are outside multiple GCM ensemble ranges (see Figure 7). This suggests
526 that the observed correlations between most climate modes of variability and SIC anomalies
527 is consistent with the CMIP6 large ensembles, within internal variability uncertainty. The far
528 stronger correlation of observations for the ATN and NPO may mean in our one realization of
529 reality these modes of variability have played a larger role than has been simulated in many
530 climate models. Again, the large spread between realizations within a large ensemble highlights
531 the extremely large range that observations would be expected to fall within (particularly for the
532 IPO), and hence the difficulty of validating the simulated low-frequency drivers with observations.

533

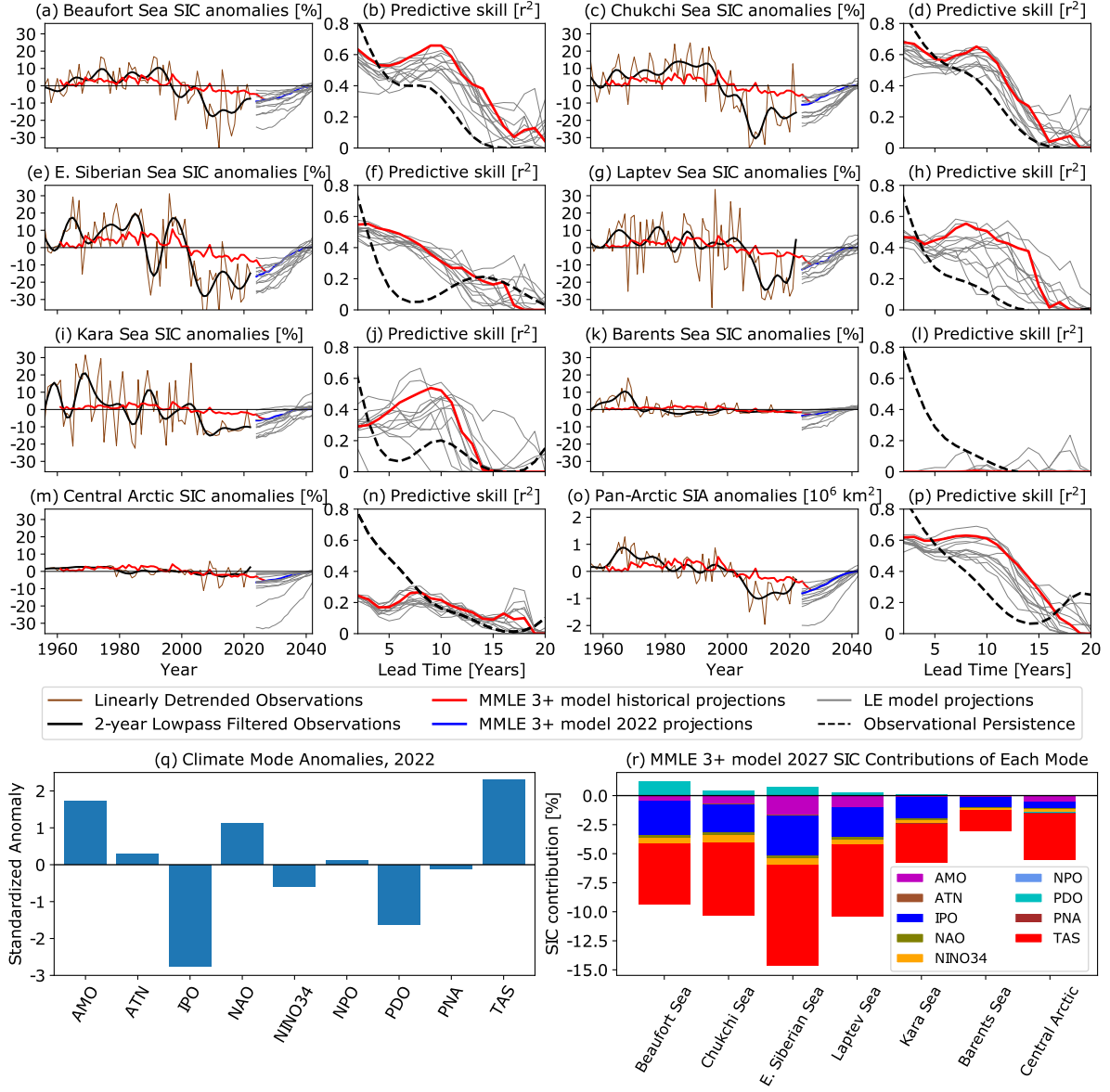


534 **FIG. 7. Correlations between ensemble members and observations between modes of variability and**
 535 **extreme SIC anomaly events.** The 6 most extreme SIC positive and negative anomalies are found for each
 536 ensemble member and September observations over the period 1956-2014. For a lead time of 4-9 years the
 537 positive and negative correlations with each mode of variability is summed. These data are the average for the
 538 Beaufort, Chukchi, East Siberian, Kara and Laptev Seas and the Central Arctic. Each colored dot indicates the
 539 correlations for a single ensemble member, with the same colored triangle indicating the ensemble mean. The
 540 observed value for each variable is shown with a black hollow bar. When observations lie within a given GCM
 541 ensemble member distribution, the correlation in the observations is consistent with that simulated in the GCM.

542 *f. Future projections*

543 Our limited time period of observations may not be representative of a typical climate
544 realization and therefore may arbitrarily match well or poorly to a specific machine learning
545 model trained on GCMs. However, validation of our LE and MMLE 3+ models against the
546 period 1956-2022 may have some implications for how well we can expect projections over the
547 next 4-20 years to hold up. The r^2 values of the MMLE 3+ validated against the observations
548 (Figure 8 prediction columns) is similar to that of the MMLE 3+ validated against the second
549 large ensemble members (Figure 3). The MMLE 3+ and the best LEs when used for hindcasting
550 SIC anomalies from observed climate modes, often achieve r^2 values of between 0.2-0.3 above
551 persistence, but is highly regionally dependent. As the MMLE 3+ typically has the highest or near
552 highest validation skill against the observations, we use these for future projections in the following.

553



554 **FIG. 8. Linear model projections of SIC anomalies based on observed climate modes.** The projection
555 subplots a,c,e,g,i,k,m,o show the observed 1956-2022 regional or pan-Arctic SIC anomalies (brown), the 2-year
556 lowpass filtered anomalies (black), the MMLE3+ linear model historical hindcasts on a 5-year lead time (red), and
557 the future projections based on the climate mode anomalies observed in 2022 using the MMLE 3+ (blue) and
558 individual LEs (grey). The prediction skill subplots b,d,f,h,j,l,n,p show the observed persistence in dashed back
559 lines while the MMLE 3+ and LE hindcast performances for 1976-2022 at 2- to 20- year lead times are shown
560 in red and gray, respectively. The subplot q depicts the observed climate mode anomalies for the year 2022.
561 Subplot r shows the MMLE 3+ contribution to the projected anomalies in 2027 based on 2022 data of each of
562 the modes of variability.

563 For all regions of the Arctic, our linear model predicts below trend sea ice concentrations
564 over the coming decade. The seven regions have different time evolutions of the projected SIC
565 anomalies, however all regions for the MMLE 3+ projections show accelerated SIC loss due to
566 low-frequency variability over the 20 years following 2022 (see Figure 8). Taking the pan-Arctic
567 as a whole, the predicted negative anomaly from the linear trend is the largest anomaly at a
568 5-year lead time during the period 1956-2022. Therefore, our MMLE 3+ model predicts current
569 climate modes as being particularly conducive to a large low-frequency SIC anomaly. This is
570 fairly consistent across LEs, with the only large outlier being the CESM2-LENS which predicts
571 an extreme accelerated loss due to being a large outlier in Central Arctic projections. This
572 outlier is likely due to thin biased ice as discussed in section 3d. Comparing the persistence
573 of CESM2-LENS with CESM2-lessmelt runs which have thicker sea ice (Kay et al. 2022), the
574 lessmelt CESM2 variant is more in line with the persistence in other GCMs (see Figure S4).
575 This indicates the low thickness bias likely caused the enhanced simulated variability outlier.

576

577 The contributions to this predicted accelerated SIC loss throughout the Arctic in the coming
578 decade is dominated by the large anomalies in 2022 of a negative IPO and strongly positive AMO,
579 alongside a moderately negative NINO34 value. Furthermore, the above trend surface temperature
580 warming in 2022 is also modeled as being a large contribution in the year 2027 (see Figure 8q,r).
581 Only the negative phase of the PDO in 2022 is expected to counter the accelerated sea ice loss by
582 leading to positive SIC anomalies in the Pacific sector. The remaining modes of variability are
583 either in near neutral phase in 2022 or have small influences on the linear model and hence do not
584 feature as contributing to future anomalies. The alignment of modes of variability phases in 2022
585 combine to simulate a negative anomaly to the linear trend larger than any anomaly predicted during
586 the period 1956-2021. Even if for example there were a sudden switch in phase of the NINO 3.4
587 index from -0.8 in 2022 to +2.0 standard deviation, the SIC % point influence in the East Siberian
588 sea would change the projected 2027 contribution from -0.78% to 1.89%. The more dominant
589 modes of variability, namely the IPO and AMO as well as the TAS influence, transition phase
590 more slowly, which would therefore reduce the sensitivity of projections based on a single year.

591

592 **4. Discussion**

593 Skillful projections of regional Arctic SIC anomalies are able to be produced using simple linear
594 relationships. This has allowed us to identify the individual impact of the dominant modes of
595 variability, namely the IPO, NINO34 and the AMO. However, covariance between the climate
596 modes of variability and nonlinearities in their effect on sea ice are likely to exist (e.g. Heo et al.
597 2021). This is also supported by the fact that many of the climate modes of variability are not
598 spatially or temporally independent of one another, such as the PDO and NINO34 (Chen and
599 Wallace 2016). The lack of improvement in skill when we included nonlinearities or covariance
600 in our analysis may be a result of a lack of data (see section 3a), despite the quantity and quality
601 of GCM data available from CMIP6 simulations being unprecedented (Davy and Outten 2020).
602 The multimodal ensemble approach to learning the drivers of Arctic sea ice variability did not
603 degrade our skill when compared with training our linear model on a single GCM (see section
604 3d). This shows that a generalized model can be obtained from a variety of GCMs differing in
605 model physics, model biases and ocean states. However, large differences in validation between
606 realizations indicates the extent to which the linear relationships themselves can differ due to
607 internal variability.

608 Previous studies have primarily focused on seasonal or interannual timescales of variability,
609 with the notable exceptions of the IPO and AMO which have been considered on decadal
610 timescales. As these modes of variability persist in one phase for several years to decades it
611 is unsurprising for their influence on sea ice to also persist with a slow near-monotonic decay
612 with time. We found the IPO to be the most influential mode of variability on all lead times
613 between 4 and 20 years, positively correlated with SIC anomalies in all regions. In previous
614 research the IPO's influence on Arctic sea ice has not been featured, except as found by Screen
615 and Deser 2019 for the CMIP5 GCM CESM1. The transition between the negative and positive
616 IPO phase in CESM1 was found to be associated with a strengthened Aleutian Low which
617 enhances poleward heat and moisture transports, facilitating enhanced Arctic sea ice loss. The
618 disagreement in sign and longevity of the IPO's influence on SIC between the CMIP6 LEs follows
619 on from research that CMIP5 GCMs generally poorly simulate the extratropical effects of the IPO
620 (Baxter et al. 2019; Ding et al. 2019; Topál et al. 2020). In addition to the lack of consensus

621 between GCMs broadly, the correlation appears highly sensitive to realization (see Figure 7).
622 Previous studies have suggested the variability in the strength of the Pacific-Arctic (PARC)
623 teleconnection may cause the linkages between Pacific SST anomalies and Arctic sea ice to vary
624 substantially and even change sign depending on initial climate state (Bonan and Blanchard-
625 Wrigglesworth 2020). Additional focus on this mode with a wider variety of modeling applications
626 appears needed and is particularly pressing given the strong current negative phase (see Figure 8q).

627

628 The AMO was found in our MMLE 3+ linear model to be negatively correlated with all
629 regions of the Arctic sea ice, which shows good agreement with previous studies (e.g. Day
630 et al. 2012; Miles et al. 2014; Li et al. 2018b) for the pan-Arctic or Atlantic sector on decadal
631 timescales. The suggested physical mechanism for a positive AMO leading sea ice loss is the
632 enhanced winter atmospheric heat transport into the Atlantic sector of the Arctic (Day et al.
633 2012). However, the AMO itself may have a forced component (Murphy et al. 2021; Cai et al.
634 2021; Klavans et al. 2022), and its oscillatory timescale varies considerably between GCMs
635 (Lee et al. 2021), potentially limiting the use of the AMO as an independent variable. Despite
636 this, the pre-industrial control simulations (see Figure S2) match well with the MMLE 3+ for
637 1920-2014 for the IPO and AMO, suggesting that forcing context is not highly important for
638 these modes. A much smaller influence of the NINO34 in the pre-industrial control simulations
639 may suggest sensitivity to climate state. Similarly the selection of the dominant season based
640 on the LEs in the period 1920-2014 could also cause an array of responses in different climate
641 conditions and for different GCMs if they simulate other seasons as being most influential.

642

643 El Niño and La Niña have been shown to be influential on Arctic sea ice and generally suggest
644 that NINO34 is positively correlated with SIC except for the Beaufort Sea (e.g. Clancy et al.
645 2021; Hu et al. 2016; Jeong et al. 2022b). However, the lead times considered previously were
646 shorter than our 4- to 20-year timescale, making our positively correlated influence hard to directly
647 compare with previous research. Furthermore, previous literature on shorter timescales have noted
648 the importance of the type of El Niño regime (Jeong et al. 2022a; Lee et al. 2023) and the likely
649 nonlinear and asymmetrical climate response from NINO34 variations (Hoerling et al. 1997).
650 Limitations to the detection of lagged influence from ENSO could be derived from the fact that

651 CMIP6 GCMs still fail to accurately simulate the periodicity and phase-locking characteristics of
652 ENSO (Hou and Tang 2022). Nonetheless, El Niño favoring a positive Arctic Oscillation and a
653 deepened Aleutian Low via Rossby wave trains, which in turn promote enhanced sea ice export,
654 have been shown to exist in a number of CMIP5 and CMIP6 GCMs (Clancy et al. 2021; Lee et al.
655 2023). What remains elusive is the persistence of the influence of the NINO34 on sea ice across
656 GCMs up to approximately 14 years (Figure 4). This is surprising due to the transition between
657 phases often occurring interannually, which would therefore require persistent lagged telecon-
658 nection pathway to the Arctic which has not been suggested. During 1970-2014 when radiative
659 forcing increase was more linear compared with 1920-2014, we found NINO34 still has a positive
660 correlation on sea ice, but only for approximately 5 years (Figure S1). For pre-industrial control
661 simulations, a constant near zero relationship was found (Figure S2). It would therefore appear that
662 for periods when nonlinearities in radiative forcing is more effectively removed by detrending or
663 by constant forcing, the lagged NINO34 influence sea ice is substantially reduced. As no physical
664 mechanism for a lagged sea ice response to a given phase of NINO34 is suggested, the influence
665 of NINO34 encapsulating residuals in the model or nonlinearities in warming must be considered.

666

667 The PDO was previously not found to be highly important for Arctic sea ice by itself (Zhang et al.
668 2020; Karami et al. 2023) and its influence may also have changed over time (Bonan and Blanchard-
669 Wrigglesworth 2020; Kim et al. 2020). Similarly we also only found a small influence of the PDO
670 over our long time period of 1920-2014. The SST pattern of the PDO is related to the Pacific SST
671 climate modes of the NINO34 and IPO, which each have similar teleconnection mechanisms via
672 Rossby wave train formation (Yuan et al. 2018). Further, the mechanisms of an oceanic 'tunnel'
673 and atmospheric 'bridge' may be common between the IPO and PDO, leading to the similar
674 characteristics of persistence, Arctic influence, and modulation by ENSO (Liu and Alexander 2007;
675 Henley et al. 2017). Therefore it is unsurprising for a subset of tropical Pacific modes of variability
676 to dominate due to their similarity. The ATN is the only negligible mode of variability derived from
677 SSTs, but has not previously been identified as specific driver of Arctic sea ice variability. However
678 the tropical Atlantic was been suggested to influence Arctic sea ice (Meehl et al. 2018). Thus, the
679 unimportant nature of the ATN does not preclude other aspects of tropical Atlantic being important.

680

681 Consistent with the previous lack of evidence of influence beyond interannual timescales, the sea
682 level pressure-derived modes of variability (the NAO, NPO and PNA) were found to have negligible
683 effect at lead times of 4-20 years. Previous research has shown the effect of the NAO to decay to
684 zero after approximately 2 years (Ukita et al. 2007), this timescale and the regional correlations
685 (e.g. Serreze et al. 2007; Döscher et al. 2010) align with our findings given the smoothing inherent
686 in our lowpass filtered data. This provides confidence in our linear model's ability to capture
687 higher frequency variability but dismiss low-frequency influence from these modes of variability.

688

689 5. Conclusions

690 We have shown that low-frequency variability of regional Arctic sea ice concentration can be
691 modeled using linear drivers consisting of climate modes of variability. We achieve predictions
692 superior to persistence for most regions for a lead time of 4-20 years and find that the climate
693 modes of variability can be considered independently without reducing skill. By comparing the
694 linear responses between twelve large ensembles from CMIP6 and a multi-model large ensemble
695 comprising of 42 GCMs, we find where there is consensus of the dominant linear drivers of
696 low-frequency sea ice variability except in the case of the Interdecadal Pacific Oscillation (IPO). In
697 the pan-Arctic we are able to explain up to 60% of observed low-frequency sea ice concentration
698 variability at lead times of 5 years. However, the ability of a GCM or a multi-model large
699 ensemble to predict unseen ensemble members or observations can vary wildly depending on the
700 realization of internal variability; between 0-0.46 r^2 in the case of CanESM5, the largest single
701 GCM ensemble. Hence, this both complicates the analysis of small samples of GCMs and the
702 application and verification of these relationships with our single realization of observations.

703

704 The most important modes of variability we found were the IPO, Nino 3.4 Index (NINO34)
705 and the Atlantic Multidecadal Oscillation (AMO). The multi-model large ensemble linear model
706 showed the IPO to have a strong positive correlation with this being most pronounced in the
707 East Siberian, Beaufort and Laptev Seas at lead times of up to 14 years. Although this large
708 magnitude of influence of the IPO was found across GCMs, the sign and regional influence

709 was especially dependent on the GCM used and the specific realization of internal variability.
710 NINO34 was found to be positively correlated with SIC anomalies in all regions, particularly
711 in the Pacific sector. This correlation was more consistent between GCMs, with disagreement
712 growing at longer lead-times. The AMO was the only other mode of variability considered
713 important for long periods of time, being modeled as highly negatively correlated with SIC
714 across all regions for up to approximately 10 years. However, the agreement across CMIP6
715 GCMs for the AMO was less consistent than NINO34. The persistence of influence on sea ice
716 from the IPO and AMO is not surprising due to their similar phase persistence. NINO34 in
717 contrast can change phase interannually, suggesting the influence found here may be an artifact
718 of forcing conditions, as no physical mechanism for a delayed Arctic influence has been suggested.

719

720 When using our linear model to make predictions, we find a near 'perfect storm' of modes of
721 variability in the year 2021/2022 to induce an acceleration to the sea ice loss trend over the next
722 decade. The primary influences of this projected acceleration of low-frequency variability driven
723 sea ice loss are an above trend global average surface temperature warming, a negative IPO, La
724 Niña conditions, and a positive AMO. For the pan-Arctic, the projected low-frequency deviation
725 from the long-term trend due to current climate mode phase configurations is expected to be the
726 largest since at least 1956. While the transition between La Niña and El Niño can occur rapidly,
727 the fact that our strong negative predictions are primarily due to the slowly changing climate
728 modes of the AMO and IPO imply robustness of this prediction to interannual variability. Of
729 course, the sea ice anomalies that will actually be observed are still dominated by interannual
730 variability, which makes up roughly three quarters of the total variability. Thus, while we cannot
731 say with confidence that a new record low September extent will occur over the next decade, the
732 modeled low-frequency variability suggests that extreme low SIC values will be more likely over
733 the coming decade, with low-frequency variability likely to enhance the long-term negative trend.

734

735 *Acknowledgments.* This work was supported by the National Science Foundation under grant
736 number 1847398. A. Jahn’s contribution was also supported by an Alexander von Humboldt
737 fellowship. We would also like to acknowledge high-performance computing on Cheyenne
738 (doi:10.5065/D6RX99HX) provided by NCAR’s Computational and Information Systems Lab-
739 oratory, sponsored by the National Science Foundation. Further, we thank Adam Philips for
740 processing updates to the Climate Variability Diagnostics Package output used in this analysis. We
741 also thank Elizabeth Barnes and David Hall for useful conversations in the early part of the project.

742 *Data availability statement.* The data used in this study is freely available at [https://esgf-
743 node.llnl.gov/projects/cmip6/](https://esgf-node.llnl.gov/projects/cmip6/) for the CMIP6 global climate model data except for the
744 CESM2-LENS, which is available at <https://www.cesm.ucar.edu/community-projects/lens2/>
745 data-
746 sets. The CVDP data is available at <https://www.cesm.ucar.edu/projects/cvdp/> data-
747 repository. The observational sea ice concentration data is freely available from
748 <https://nsidc.org/data/g02202/versions/4>. All code required to replicate this study is archived
749 at Zenodo at <https://doi.org/10.5281/zenodo.12580233>. Additionally the linear model coefficients
750 and the observational CVDP output data processed for this analysis is available via the Arctic Data
Center at <https://doi.org/10.18739/A2MS3K35M>.

751 **References**

752 Alexander, M. A., I. Bladé, M. Newman, J. R. Lanzante, N.-C. Lau, and J. D. Scott, 2002:
753 The atmospheric bridge: The influence of enso teleconnections on air–sea interaction over
754 the global oceans. *Journal of Climate*, **15**, 2205 – 2231, [https://doi.org/https://doi.org/10.1175/1520-0442\(2002\)015<2205:TABTIO>2.0.CO;2](https://doi.org/https://doi.org/10.1175/1520-0442(2002)015<2205:TABTIO>2.0.CO;2).

755

756 Bader, D. C., R. Leung, M. Taylor, and R. B. McCoy, 2019: E3SM-Project E3SM1.0 model
757 output prepared for CMIP6 CMIP historical. Earth System Grid Federation, <https://doi.org/10.22033/ESGF/CMIP6.4497>.

758

759 Barnes, E. A., J. W. Hurrell, I. Ebert-Uphoff, C. Anderson, and D. Anderson, 2019: Viewing
760 Forced Climate Patterns Through an AI Lens. *Geophysical Research Letters*, **46**, 13 389–13 398,
761 <https://doi.org/10.1029/2019GL084944>.

762

763 Barnhart, K. R., C. R. Miller, I. Overeem, and J. E. Kay, 2016: Mapping the future expansion of
Arctic open water. *Nature Climate Change*, **6**, 280–285, <https://doi.org/10.1038/nclimate2848>.

764

765 Baxter, I., and Coauthors, 2019: How tropical Pacific surface cooling contributed to accelerated
766 sea ice melt from 2007 to 2012 as ice is thinned by anthropogenic forcing. *Journal of Climate*,
32 (24), 8583–8602, <https://doi.org/10.1175/JCLI-D-18-0783.1>.

767

768 Bentsen, M., and Coauthors, 2019: NCC NorESM2-MM model output prepared for CMIP6 CMIP
historical. Earth System Grid Federation, <https://doi.org/10.22033/ESGF/CMIP6.8040>.

769

770 Bethke, I., and Coauthors, 2019: NCC NorCPM1 model output prepared for CMIP6 CMIP
historical. Earth System Grid Federation, <https://doi.org/10.22033/ESGF/CMIP6.10894>.

771

772 Bethke, I., and Coauthors, 2021: NorCPM1 and its contribution to CMIP6 DCPP. *Geoscientific
Model Development*, **14**, 7073–7116, <https://doi.org/10.5194/gmd-14-7073-2021>.

773

774 Blanchard-Wrigglesworth, E., K. C. Armour, C. M. Bitz, and E. Deweaver, 2011: Persistence
775 and inherent predictability of Arctic sea ice in a GCM ensemble and observations. *Journal of
Climate*, **24**, 231–250, <https://doi.org/10.1175/2010JCLI3775.1>.

776

777 Blanchard-Wrigglesworth, E., and M. Bushuk, 2019: Robustness of Arctic sea-ice predictability
in GCMs. *Climate Dynamics*, **52**, 5555–5566, <https://doi.org/10.1007/s00382-018-4461-3>.

778 Bonan, D. B., and E. Blanchard-Wrigglesworth, 2020: Nonstationary teleconnection between
779 the pacific ocean and arctic sea ice. *Geophysical Research Letters*, **47**, e2019GL085 666,
780 <https://doi.org/10.1029/2019GL085666>.

781 Bonan, D. B., M. Bushuk, and M. Winton, 2019: A spring barrier for regional predictions of
782 summer arctic sea ice. *Geophysical Research Letters*, **46**, 5937–5947, <https://doi.org/10.1029/2019GL082947>.

783

784 Bonan, D. B., F. Lehner, and M. M. Holland, 2021: Partitioning uncertainty in projections of
785 Arctic sea ice. *Environmental Research Letters*, **16**, <https://doi.org/10.1088/1748-9326/abe0ec>.

786 Boucher, O., and Coauthors, 2018: IPSL IPSL-CM6A-LR model output prepared for CMIP6
787 CMIP historical. Earth System Grid Federation, <https://doi.org/10.22033/ESGF/CMIP6.5195>.

788 Brown, J. R., and Coauthors, 2020: Comparison of past and future simulations of ENSO in
789 CMIP5/PMIP3 and CMIP6/PMIP4 models. *Climate of the Past*, **16**, 1777–1805, <https://doi.org/10.5194/cp-16-1777-2020>.

790

791 Bushuk, M., and D. Giannakis, 2017: The seasonality and interannual variability of Arctic Sea ice
792 reemergence. *Journal of Climate*, **30**, 4657–4676, <https://doi.org/10.1175/JCLI-D-16-0549.1>.

793 Bushuk, M., R. Msadek, M. Winton, G. Vecchi, X. Yang, A. Rosati, and R. Gudgel, 2019: Regional
794 arctic sea–ice prediction: potential versus operational seasonal forecast skill. *Climate Dynamics*,
795 **52**, 2721–2743, <https://doi.org/10.1007/S00382-018-4288-Y/FIGURES/11>.

796 Cai, Q., D. Beletsky, J. Wang, and R. Lei, 2021: Interannual and decadal variability of arctic
797 summer sea ice associated with atmospheric teleconnection patterns during 1850–2017. *Journal
798 of Climate*, **34**, 9931–9955, <https://doi.org/10.1175/JCLI-D-20-0330.1>.

799

800 Cao, J., and B. Wang, 2019: NUIST NESMv3 model output prepared for CMIP6 CMIP historical.
Earth System Grid Federation, <https://doi.org/10.22033/ESGF/CMIP6.8769>.

801 Chen, X., and J. M. Wallace, 2016: Orthogonal pdo and enso indices. *Journal of Climate*, **29 (10)**,
802 3883–3892, <https://doi.org/10.1175/JCLI-D-15-0684.1>.

803 Clancy, R., C. Bitz, and E. Blanchard-Wrigglesworth, 2021: The Influence of ENSO on Arctic Sea
804 Ice in Large Ensembles and Observations. *Journal of Climate*, **34**, 9585–9604, <https://doi.org/10.1175/JCLI-D-20-0958.1>.

805

806 Crawford, A., J. Stroeve, A. Smith, and A. Jahn, 2021: Arctic open-water periods are projected
807 to lengthen dramatically by 2100. *Communications Earth and Environment*, **2**, <https://doi.org/10.1038/s43247-021-00183-x>.

808

809 Dalelane, C., K. Winderlich, and A. Walter, 2023: Evaluation of global teleconnections in CMIP6
810 climate projections using complex networks. *Earth System Dynamics*, **14**, 17–37, <https://doi.org/10.5194/esd-14-17-2023>.

811

812 Danabasoglu, G., 2019a: NCAR CESM2-FV2 model output prepared for CMIP6 CMIP historical.
813 Earth System Grid Federation, <https://doi.org/10.22033/ESGF/CMIP6.11297>.

814

815 Danabasoglu, G., 2019b: NCAR CESM2 model output prepared for CMIP6 CMIP historical.
Earth System Grid Federation, <https://doi.org/10.22033/ESGF/CMIP6.7627>.

816

817 Danabasoglu, G., 2019c: NCAR CESM2-WACCM-FV2 model output prepared for CMIP6 CMIP
historical. Earth System Grid Federation, <https://doi.org/10.22033/ESGF/CMIP6.11298>.

818

819 Danabasoglu, G., 2019d: NCAR CESM2-WACCM model output prepared for CMIP6 CMIP
historical. Earth System Grid Federation, <https://doi.org/10.22033/ESGF/CMIP6.10071>.

820

821 Davy, R., and S. Outten, 2020: The Arctic surface climate in CMIP6: Status and developments
since CMIP5. *Journal of Climate*, **33**, 8047–8068, <https://doi.org/10.1175/JCLI-D-19-0990.1>.

822

823 Day, J. J., J. C. Hargreaves, J. D. Annan, and A. Abe-Ouchi, 2012: Sources of multi-decadal
variability in Arctic sea ice extent. *Environmental Research Letters*, **7**, <https://doi.org/10.1088/1748-9326/7/3/034011>.

824

825 Day, J. J., E. Hawkins, and S. Tietsche, 2014: Will Arctic sea ice thickness initialization improve
826 seasonal forecast skill? *Geophysical Research Letters*, **41** (21), 7566–7575, <https://doi.org/10.1002/2014GL061694>.

827

828 Deser, C., and Coauthors, 2020: Insights from Earth system model initial-condition large en-
829 sembles and future prospects. *Nature Climate Change*, **10**, 277–286, <https://doi.org/10.1038/s41558-020-0731-2>.

831 Diffenbaugh, N. S., and E. A. Barnes, 2023: Data-driven predictions of the time remaining until
832 critical global warming thresholds are reached. *Proceedings of the National Academy of Sciences
833 of the United States of America*, **120**, <https://doi.org/10.1073/pnas.2207183120>.

834 Ding, Q., and Coauthors, 2019: Fingerprints of internal drivers of Arctic sea ice loss in ob-
835 servations and model simulations. *Nature Geoscience*, **12**, 28–33, <https://doi.org/10.1038/s41561-018-0256-8>.

837 Dix, M., and Coauthors, 2019: CSIRO-ARCCSS ACCESS-CM2 model output prepared for CMIP6
838 CMIP historical. Earth System Grid Federation, <https://doi.org/10.22033/ESGF/CMIP6.4271>.

839 Docquier, D., T. Koenigk, R. Fuentes-Franco, M. P. Karami, and Y. Ruprich-Robert, 2021: Impact
840 of ocean heat transport on the Arctic sea-ice decline: a model study with EC-Earth3. *Climate
841 Dynamics*, **56**, 1407–1432, <https://doi.org/10.1007/s00382-020-05540-8>.

842 Döscher, R., K. Wyser, H. E. Meier, M. Qian, and R. Redler, 2010: Quantifying Arctic contributions
843 to climate predictability in a regional coupled ocean-ice-atmosphere model. *Climate Dynamics*,
844 **34** (7), 1157–1176, <https://doi.org/10.1007/s00382-009-0567-y>.

845 DuVivier, A. K., M. M. Holland, J. E. Kay, S. Tilmes, A. Gettelman, and D. A. Bailey, 2020:
846 Arctic and Antarctic Sea Ice Mean State in the Community Earth System Model Version 2
847 and the Influence of Atmospheric Chemistry. *Journal of Geophysical Research: Oceans*, **125**,
848 <https://doi.org/10.1029/2019JC015934>.

849 Dörr, J., D. B. Bonan, M. Årthun, L. Svendsen, and R. C. J. Wills, 2023: Forced and in-
850 internal components of observed Arctic sea-ice changes. *The Cryosphere*, **17** (9), 4133–4153,
851 <https://doi.org/10.5194/tc-17-4133-2023>.

852 EC-Earth-Consortium, 2019a: EC-Earth-Consortium EC-Earth3 model output prepared for
853 CMIP6 CMIP historical. Earth System Grid Federation, <https://doi.org/10.22033/ESGF/CMIP6.4700>.

855 EC-Earth-Consortium, 2019b: EC-Earth-Consortium EC-Earth3-Veg model output prepared for
856 CMIP6 CMIP historical. Earth System Grid Federation, <https://doi.org/10.22033/ESGF/CMIP6.4706>.

858 EC-Earth-Consortium, 2020: EC-Earth-Consortium EC-Earth3-Veg-LR model output prepared
859 for CMIP6 CMIP historical. Earth System Grid Federation, <https://doi.org/10.22033/ESGF/CMIP6.4707>.

861 EC-Earth-Consortium, 2021: EC-Earth-Consortium EC-Earth-3-CC model output prepared for
862 CMIP6 CMIP historical. Earth System Grid Federation, <https://doi.org/10.22033/ESGF/CMIP6.4702>.

864 Eguíluz, V. M., J. Fernández-Gracia, X. Irigoien, and C. M. Duarte, 2016: A quantitative as-
865 sessment of Arctic shipping in 2010–2014. *Scientific Reports* 2016 6:1, **6**, 1–6, <https://doi.org/10.1038/srep30682>.

867 Eisenman, I., 2010: Geographic muting of changes in the arctic sea ice cover. *Geophysical Research
868 Letters*, **37**, <https://doi.org/10.1029/2010GL043741>.

869 England, M., A. Jahn, and L. Polvani, 2019: Nonuniform contribution of internal vari-
870 ability to recent Arctic sea ice loss. *Journal of Climate*, **32**, 4039–4053, <https://doi.org/10.1175/JCLI-D-18-0864.1>.

872 Fasullo, J. T., A. S. Phillips, and C. Deser, 2020: Evaluation of Leading Modes of Climate
873 Variability in the CMIP Archives. *Journal of Climate*, **33**, 5527–5545, <https://doi.org/10.1175/jcli-d-19-1024.1>.

875 Fetterer, F., M. Savoie, S. Helfrich, and P. Clemente-Colón, 2010: Multisensor Analyzed Sea Ice
876 Extent - Northern Hemisphere (MASIE-NH), Version 1. *U.S. National Ice Center and National
877 Snow and Ice Data Center*, <https://doi.org/10.7265/N5GT5K3K>.

878 Francis, J. A., and B. Wu, 2020: Why has no new record-minimum Arctic sea-ice extent occurred
879 since September 2012? *Environmental Research Letters*, **15**, <https://doi.org/10.1088/1748-9326/abc047>.

881 Furtado, J. C., E. D. Lorenzo, B. T. Anderson, and N. Schneider, ??: <https://doi.org/10.1007/s00382-011-1245-4>.

883 Giesse, C., D. Notz, and J. Baehr, 2021: On the Origin of Discrepancies Between Observed
884 and Simulated Memory of Arctic Sea Ice. *Geophysical Research Letters*, **48**, <https://doi.org/10.1029/2020GL091784>.

886 Goosse, H., O. Arzel, C. M. Bitz, A. D. Montety, and M. Vancoppenolle, 2009: Increased variability
887 of the Arctic summer ice extent in a warmer climate. *Geophysical Research Letters*, **36**, 1–5,
888 <https://doi.org/10.1029/2009GL040546>.

889 Gregory, W., J. Stroeve, and M. Tsamados, 2021: Network connectivity between the winter Arctic
890 Oscillation and summer sea ice in CMIP6 models and observations. *The Cryosphere*, 1653–1673.

891 Guemas, V., and Coauthors, 2016: A review on Arctic sea-ice predictability and prediction on
892 seasonal to decadal time-scales. *Quarterly Journal of the Royal Meteorological Society*, **142**,
893 546–561, <https://doi.org/10.1002/qj.2401>.

894 Hajima, T., and Coauthors, 2019: MIROC MIROC-ES2L model output prepared for CMIP6 CMIP
895 historical. Earth System Grid Federation, <https://doi.org/10.22033/ESGF/CMIP6.5602>.

896 Henley, B. J., and Coauthors, 2017: Spatial and temporal agreement in climate model simulations
897 of the Interdecadal Pacific Oscillation. *Environmental Research Letters*, **12**, <https://doi.org/10.1088/1748-9326/aa5cc8>.

898 899 Heo, E. S., M. K. Sung, S. I. An, and Y. M. Yang, 2021: Decadal phase shift of summertime Arctic
900 dipole pattern and its nonlinear effect on sea ice extent. *International Journal of Climatology*,
901 **41**, 4732–4742, <https://doi.org/10.1002/joc.7097>.

902 Hoerling, M. P., A. Kumar, and M. Zhong, 1997: El Niño, La Niña, and the Nonlinearity of Their
903 Teleconnections. *Journal of Climate*, **10** (8), 1769–1786, [https://doi.org/10.1175/1520-0442\(1997\)010<1769:ENOLNA>2.0.CO;2](https://doi.org/10.1175/1520-0442(1997)010<1769:ENOLNA>2.0.CO;2).

904 905 Hofsteenge, M. G., R. G. Graversen, J. H. Rydsaa, and Z. Rey, 2022: The impact of atmospheric
906 Rossby waves and cyclones on the Arctic sea ice variability. *Climate Dynamics*, **59**, 579–594,
907 <https://doi.org/10.1007/s00382-022-06145-z>.

908 Holland, M. M., L. Landrum, D. Bailey, and S. Vavrus, 2019: Changing seasonal predictability
909 of Arctic summer sea ice area in a warming climate. *Journal of Climate*, **32**, 4963–4979,
910 <https://doi.org/10.1175/jcli-d-19-0034.1>.

911 Hou, M., and Y. Tang, 2022: Recent progress in simulating two types of ENSO – from CMIP5 to
912 CMIP6. *Frontiers in Marine Science*, **9**, <https://doi.org/10.3389/fmars.2022.986780>.

913 Hu, C., S. Yang, Q. Wu, Z. Li, J. Chen, K. Deng, T. Zhang, and C. Zhang, 2016: Shifting El
914 Niño inhibits summer Arctic warming and Arctic sea-ice melting over the Canada Basin. *Nature
915 Communications*, **7**, 1–9, <https://doi.org/10.1038/ncomms11721>.

916 Huang, W., 2019: THU CIESM model output prepared for CMIP6 CMIP historical. Earth System
917 Grid Federation, <https://doi.org/10.22033/ESGF/CMIP6.8843>.

918 Hurrell, J. W., and C. Deser, 2009: North Atlantic climate variability: The role of the North Atlantic
919 Oscillation. *Journal of Marine Systems*, **78** (1), 28–41, <https://doi.org/10.1016/j.jmarsys.2008.11.026>, URL <http://dx.doi.org/10.1016/j.jmarsys.2008.11.026>.

920 Jahn, A., 2018: Reduced probability of ice-free summers for 1.5 °c compared to 2 °c warming.
921 *Nature Climate Change*, **8**, 409–413, <https://doi.org/10.1038/s41558-018-0127-8>.

922 Jeong, H., H.-S. Park, M. F. Stuecker, and S.-W. Yeh, 2022a: Distinct impacts of major El
923 Niño events on Arctic temperatures due to differences in eastern tropical Pacific sea surface
924 temperatures. *Sci. Adv.*, **8**, 8278.

925 Jeong, H., H. S. Park, M. F. Stuecker, and S. W. Yeh, 2022b: Record Low Arctic Sea Ice Extent
926 in 2012 Linked to Two-Year La Niña-Driven Sea Surface Temperature Pattern. *Geophysical
927 Research Letters*, **49**, <https://doi.org/10.1029/2022GL098385>.

928 Kalnay, E., and Coauthors, 1996: The NCEP/NCAR 40-Year Reanalysis Project. *Bulletin of
929 the American Meteorological Society*, **77**, 437–471, [https://doi.org/10.1175/1520-0477\(1996\)077<0437:TNYRP>2.0.CO;2](https://doi.org/10.1175/1520-0477(1996)
930 077<0437:TNYRP>2.0.CO;2).

931 Karami, M. P., T. Koenigk, and B. Tremblay, 2023: Variability modes of September Arctic sea ice:
932 drivers and their contributions to sea ice trend and extremes. *Environmental Research: Climate*,
933 **2**, 025 005, <https://doi.org/10.1088/2752-5295/accbe3>.

934 Kay, J. E., M. M. Holland, and A. Jahn, 2011: Inter-annual to multi-decadal Arctic sea ice extent
935 trends in a warming world. *Geophysical Research Letters*, **38**, 2–7, [https://doi.org/10.1029/2011GL048008](https://doi.org/10.1029/
936 2011GL048008).

937

938 Kay, J. E., and Coauthors, 2022: Less Surface Sea Ice Melt in the CESM2 Improves Arctic Sea Ice
939 Simulation With Minimal Non-Polar Climate Impacts. *Journal of Advances in Modeling Earth*
940 *Systems*, **14**, <https://doi.org/10.1029/2021MS002679>.

941 Kim, H., S. W. Yeh, S. I. An, and S. Y. Song, 2020: Changes in the role of Pacific decadal oscillation
942 on sea ice extent variability across the mid-1990s. *Scientific Reports*, **10**, <https://doi.org/10.1038/s41598-020-74260-0>.

944 Klavans, J. M., M. A. Cane, A. C. Clement, and L. N. Murphy, 2021: NAO predictability from
945 external forcing in the late 20th century. *npj Climate and Atmospheric Science* 2021 **4**:1, **4**, 1–8,
946 <https://doi.org/10.1038/s41612-021-00177-8>.

947 Klavans, J. M., A. C. Clement, M. A. Cane, and L. N. Murphy, 2022: The Evolving Role of External
948 Forcing in North Atlantic SST Variability over the Last Millennium. *Journal of Climate*, **35**,
949 2741–2754, <https://doi.org/10.1175/JCLI-D-21-0338.1>.

950 Knutti, R., D. Masson, and A. Gettelman, 2013: Climate model genealogy: Generation CMIP5
951 and how we got there. *Geophysical Research Letters*, **40**, 1194–1199, <https://doi.org/10.1002/grl.50256>.

953 Kovacs, K. M., C. Lydersen, J. E. Overland, and S. E. Moore, 2011: Impacts of changing sea-
954 ice conditions on Arctic marine mammals. *Marine Biodiversity*, **41**, 181–194, <https://doi.org/10.1007/s12526-010-0061-0>.

956 Krasting, J. P., and Coauthors, 2018: NOAA-GFDL GFDL-ESM4 model output prepared for
957 CMIP6 CMIP historical. Earth System Grid Federation, <https://doi.org/10.22033/ESGF/CMIP6.8597>.

959 Kwok, R., and D. A. Rothrock, 2009: Decline in Arctic sea ice thickness from submarine and
960 ICESat records: 1958–2008. *Geophysical Research Letters*, **36** (15), 1–5, <https://doi.org/10.1029/2009GL039035>.

962 Labe, Z. M., and E. A. Barnes, 2022: Comparison of Climate Model Large Ensembles With
963 Observations in the Arctic Using Simple Neural Networks. *Earth and Space Science*, **9**,
964 e2022EA002348, <https://doi.org/10.1029/2022EA002348>.

965 Leathers, D. J., B. Yarnal, and M. A. Palecki, 1991: The Pacific/North American Teleconnection
966 Pattern and United States Climate. Part I: Regional Temperature and Precipitation Associations.
967 *Journal of Climate*, **4**, 517 – 528, [https://doi.org/10.1175/1520-0442\(1991\)004<0517:TPATPA>2.0.CO;2](https://doi.org/10.1175/1520-0442(1991)004<0517:TPATPA>2.0.CO;2).

969 Lee, J., K. R. Sperber, P. J. Gleckler, K. E. Taylor, , Céline, and J. W. Bonfils, 2021: Benchmarking
970 Performance Changes in the Simulation of Extratropical Modes of Variability across CMIP
971 Generations. *Journal of Climate*, **34**, <https://doi.org/10.1175/JCLI-D-20>.

972 Lee, S., H. S. Park, S. Y. Song, and S. W. Yeh, 2023: Distinct impacts of two types of El
973 Niño events on northern winter high-latitude temperatures simulated by CMIP6 climate models.
974 *Environmental Research Letters*, **18**, <https://doi.org/10.1088/1748-9326/acbce9>.

975 Lenssen, N. J. L., G. A. Schmidt, J. E. Hansen, M. J. Menne, A. Persin, R. Ruedy, and D. Zyss,
976 2019: Improvements in the GISTEMP Uncertainty Model. *Journal of Geophysical Research: Atmospheres*, **124**, 6307–6326, <https://doi.org/10.1029/2018JD029522>.

978 L'Heureux, M. L., A. Kumar, G. D. Bell, M. S. Halpert, and R. W. Higgins, 2008: Role of the
979 Pacific-North American (PNA) pattern in the 2007 Arctic sea ice decline. *Geophysical Research
980 Letters*, **35**, <https://doi.org/10.1029/2008GL035205>.

981 Li, D., R. Zhang, and T. Knutson, 2018a: Comparison of Mechanisms for Low-Frequency Vari-
982 ability of Summer Arctic Sea Ice in Three Coupled Models. *Journal of Climate*, **31**, 1205–1226,
983 <https://doi.org/10.1175/JCLI-D-16-0617.1>.

984 Li, F., Y. J. Orsolini, H. Wang, Y. Gao, and S. He, 2018b: Atlantic Multidecadal Oscillation
985 Modulates the Impacts of Arctic Sea Ice Decline. *Geophysical Research Letters*, **45**, 2497–2506,
986 <https://doi.org/10.1002/2017GL076210>.

987 Lindsay, R. W., and J. Zhang, 2006: Arctic ocean ice thickness: Modes of variability and the
988 best locations from which to monitor them. *Journal of Physical Oceanography*, **36**, 496–506,
989 <https://doi.org/10.1175/JPO2861.1>.

990 Liu, Z., and M. Alexander, 2007: Atmospheric bridge, oceanic tunnel, and global climatic tele-
991 connections. <https://doi.org/10.1029/2005RG000172>.

992 Liu, Z., and Coauthors, 2021: Acceleration of western Arctic sea ice loss linked to the Pacific North
993 American pattern. *Nature Communications*, **12**, <https://doi.org/10.1038/s41467-021-21830-z>.

994 Long, M., L. Zhang, S. Hu, and S. Qian, 2021: Multi-aspect assessment of CMIP6 models for Arctic
995 sea ice simulation. *Journal of Climate*, **34**, 1515–1529, <https://doi.org/10.1175/JCLI-D-20-0522.1>.

997 Lovato, T., and D. Peano, 2020: CMCC CMCC-CM2-SR5 model output prepared for CMIP6
998 CMIP historical. Earth System Grid Federation, <https://doi.org/10.22033/ESGF/CMIP6.3825>.

999 MacDonald, G. M., and R. A. Case, 2005: Variations in the Pacific Decadal Oscillation over the past
1000 millennium. *Geophysical Research Letters*, **32**, 1–4, <https://doi.org/10.1029/2005GL022478>.

1001 Mantua, N. J., S. R. Hare, Y. Zhang, J. M. Wallace, and R. C. Francis, 1997: A pacific interdecadal
1002 climate oscillation with impacts on salmon production. *Bulletin of the American Meteorological
1003 Society*, **78**, 1069–1080, [https://doi.org/10.1175/1520-0477\(1997\)078<1069:APICOW>2.0.CO;2](https://doi.org/10.1175/1520-0477(1997)078<1069:APICOW>2.0.CO;2).

1005 McBride, L. A., A. P. Hope, T. P. Carty, B. F. Bennett, W. R. Tribett, and R. J. Salawitch,
1006 2021: Comparison of CMIP6 historical climate simulations and future projected warming to
1007 an empirical model of global climate. *Earth System Dynamics*, **12**, 545–579, <https://doi.org/10.5194/esd-12-545-2021>.

1009 Meehl, G. A., C. T. Chung, J. M. Arblaster, M. M. Holland, and C. M. Bitz, 2018: Tropical
1010 Decadal Variability and the Rate of Arctic Sea Ice Decrease. *Geophysical Research Letters*, **45**,
1011 11,326–11,333, <https://doi.org/10.1029/2018GL079989>.

1012 Meehl, G. A., A. Hu, J. M. Arblaster, J. Fasullo, and K. E. Trenberth, 2013: Externally forced
1013 and internally generated decadal climate variability associated with the interdecadal pacific
1014 oscillation. *Journal of Climate*, **26**, 7298–7310, <https://doi.org/10.1175/JCLI-D-12-00548.1>.

1015 Melia, N., K. Haines, E. Hawkins, and J. J. Day, 2017: Towards seasonal Arctic shipping route
1016 predictions. *Environmental Research Letters*, **12**, 084 005, <https://doi.org/10.1088/1748-9326/AA7A60>.

1018 Miles, M. W., D. V. Divine, T. Furevik, E. Jansen, M. Moros, and A. E. Ogilvie, 2014: A signal of
1019 persistent Atlantic multidecadal variability in Arctic sea ice. *Geophysical Research Letters*, **41**,
1020 463–469, <https://doi.org/10.1002/2013GL058084>.

1021 Milinski, S., N. Maher, and D. Olonscheck, 2020: How large does a large ensemble need to be?
1022 *Earth Syst. Dynam.*, **11**, 885–901, <https://doi.org/10.5194/esd-11-885-2020>.

1023 Mioduszewski, J. R., S. Vavrus, M. Wang, M. Holland, and L. Landrum, 2019: Past and future
1024 interannual variability in Arctic sea ice in coupled climate models. *Cryosphere*, **13**, 113–124,
1025 <https://doi.org/10.5194/tc-13-113-2019>.

1026 Murphy, L. N., J. M. Klavans, A. C. Clement, and M. A. Cane, 2021: Investigating the Roles
1027 of External Forcing and Ocean Circulation on the Atlantic Multidecadal SST Variability in a
1028 Large Ensemble Climate Model Hierarchy. *Journal of Climate*, 1–51, <https://doi.org/10.1175/JCLI-D-20-0167.1>.

1030 NASA Goddard Institute for Space Studies, 2018: NASA-GISS GISS-E2.1G model output prepared
1031 for CMIP6 CMIP historical. Earth System Grid Federation, <https://doi.org/10.22033/ESGF/CMIP6.7127>.

1033 NASA Goddard Institute for Space Studies, 2019a: NASA-GISS GISS-E2-2-G model output
1034 prepared for CMIP6 CMIP historical. Earth System Grid Federation, <https://doi.org/10.22033/ESGF/CMIP6.7129>.

1036 NASA Goddard Institute for Space Studies, 2019b: NASA-GISS GISS-E2.1H model output
1037 prepared for CMIP6 CMIP historical. Earth System Grid Federation, <https://doi.org/10.22033/ESGF/CMIP6.7128>.

1039 NASA Goddard Institute for Space Studies, 2019c: NASA-GISS GISS-E2.2H model out-
1040 put prepared for CMIP6 CMIP historical. Earth System Grid Federation, <https://doi.org/10.22033/ESGF/CMIP6.15871>.

1042 Neubauer, D., and Coauthors, 2019: HAMMOZ-Consortium MPI-ESM1.2-HAM model output
1043 prepared for CMIP6 CMIP historical. Earth System Grid Federation, <https://doi.org/10.22033/ESGF/CMIP6.5016>.

1045 Notz, D., 2015: How well must climate models agree with observations? *Philosophical
1046 Transactions of the Royal Society A: Mathematical, Physical and Engineering Sciences*, **373**,
1047 <https://doi.org/10.1098/rsta.2014.0164>.

1048 Notz, D., and J. Stroeve, 2016: Observed Arctic sea-ice loss directly follows anthropogenic CO₂
1049 emission. *Science*, **354**, 747–750, <https://doi.org/10.1126/science.aag2345>.

1050 Olonscheck, D., T. Mauritsen, and D. Notz, 2019: Arctic sea-ice variability is primarily driven
1051 by atmospheric temperature fluctuations. *Nature Geoscience*, **12**, 430–434, <https://doi.org/10.1038/s41561-019-0363-1>.

1053 Onarheim, I. H., T. Eldevik, L. H. Smedsrud, and J. C. Stroeve, 2018: Seasonal and regional
1054 manifestation of Arctic sea ice loss. *Journal of Climate*, **31**, 4917–4932, <https://doi.org/10.1175/JCLI-D-17-0427.1>.

1056 O’neill, B. C., and Coauthors, 2016: The Scenario Model Intercomparison Project (ScenarioMIP)
1057 for CMIP6. *Geosci. Model Dev*, **9**, 3461–3482, <https://doi.org/10.5194/gmd-9-3461-2016>.

1058 Petrick, S., K. Riemann-Campe, S. Hoog, C. Growitsch, H. Schwind, R. Gerdes, and K. Rehdanz,
1059 2017: Climate change, future Arctic Sea ice, and the competitiveness of European Arctic
1060 offshore oil and gas production on world markets. *Ambio*, **46**, 410–422, <https://doi.org/10.1007/s13280-017-0957-z>.

1062 Phillips, A., C. Deser, and J. Fasullo, 2014: A New Tool for Evaluating Modes of Variability in
1063 Climate Models. *Eos*, **95**, 453–455, <https://doi.org/10.1002/2014EO490002>.

1064 Rayner, N. A., D. E. Parker, E. B. Horton, C. K. Folland, L. V. Alexander, D. P. Rowell, E. C. Kent,
1065 and A. Kaplan, 2003: Global analyses of sea surface temperature, sea ice, and night marine air
1066 temperature since the late nineteenth century. *Journal of Geophysical Research: Atmospheres*,
1067 **108**, 4407, <https://doi.org/10.1029/2002jd002670>.

1068 Ridley, J., M. Menary, T. Kuhlbrodt, M. Andrews, and T. Andrews, 2019a: MOHC HadGEM3-
1069 GC31-LL model output prepared for CMIP6 CMIP historical. Earth System Grid Federation,
1070 <https://doi.org/10.22033/ESGF/CMIP6.6109>.

1071 Ridley, J., M. Menary, T. Kuhlbrodt, M. Andrews, and T. Andrews, 2019b: MOHC HadGEM3-
1072 GC31-MM model output prepared for CMIP6 CMIP historical. Earth System Grid Federation,
1073 <https://doi.org/10.22033/ESGF/CMIP6.6112>.

1074 Roach, L. A., and E. Blanchard-Wrigglesworth, 2022: Observed Winds Crucial for Septem-
1075 ber Arctic Sea Ice Loss. *Geophysical Research Letters*, **49** (6), 1–10, <https://doi.org/10.1029/2022GL097884>.

1077 Rogers, J. C., 1981: The North Pacific Oscillation. *Journal of Climatology*, **1** (1), 39–57,
1078 <https://doi.org/10.1002/joc.3370010106>.

1079 Rong, X., 2019: CAMS CAMS-CSM1.0 model output prepared for CMIP6 CMIP historical. Earth
1080 System Grid Federation, <https://doi.org/10.22033/ESGF/CMIP6.9754>.

1081 Schupfner, M., and Coauthors, 2019: DKRZ MPI-ESM1.2-HR model output prepared for CMIP6
1082 historical. Earth System Grid Federation, <https://doi.org/10.22033/ESGF/CMIP6.6594>.

1083 Screen, J. A., and C. Deser, 2019: Pacific Ocean Variability Influences the Time of Emergence of a
1084 Seasonally Ice-Free Arctic Ocean. *Geophysical Research Letters*, **46**, 2222–2231, <https://doi.org/10.1029/2018GL081393>.

1086 Seferian, R., 2018: CNRM-CERFACS CNRM-ESM2-1 model output prepared for CMIP6 CMIP
1087 historical. Earth System Grid Federation, <https://doi.org/10.22033/ESGF/CMIP6.4068>.

1088 Selander, y., and Coauthors, 2019: NCC NorESM2-LM model output prepared for CMIP6 CMIP
1089 historical. Earth System Grid Federation, <https://doi.org/10.22033/ESGF/CMIP6.8036>.

1090 Serreze, M. C., M. M. Holland, and J. Stroeve, 2007: Perspectives on the Arctic's Shrinking
1091 Sea-Ice Cover. *Science*, **315** (5818), 1533–1536, <https://doi.org/10.1126/science.1139426>.

1092 Sigmond, M., J. C. Fyfe, and N. C. Swart, 2018: Ice-free Arctic projections under the Paris
1093 Agreement. *Nature Climate Change*, **8**, 404–408, <https://doi.org/10.1038/s41558-018-0124-y>.

1094 Simon, A., G. Gastineau, C. Frankignoul, V. Lapin, and P. Ortega, 2022: Pacific Decadal Oscillation
1095 modulates the Arctic sea-ice loss influence on the midlatitude atmospheric circulation in winter.
1096 *Weather and Climate Dynamics*, **3**, 845–861, <https://doi.org/10.5194/wcd-3-845-2022>.

1097 Song, Z., F. Qiao, Y. Bao, Q. Shu, Y. Song, and X. Yang, 2019: FIO-QLNM FIO-ESM2.0 model
1098 output prepared for CMIP6 CMIP historical. Earth System Grid Federation, <https://doi.org/10.22033/ESGF/CMIP6.9199>.

1100 Stroeve, J., M. M. Holland, W. Meier, T. Scambos, and M. Serreze, 2007: Arctic sea
1101 ice decline: Faster than forecast. *Geophysical Research Letters*, **34**, 9501, <https://doi.org/10.1029/2007GL029703>.

1103 Swart, N. C., J. C. Fyfe, E. Hawkins, J. E. Kay, and A. Jahn, 2015: Influence of internal variability
1104 on arctic sea-ice trends. *Nature Climate Change*, **5**, 86–89, <https://doi.org/10.1038/nclimate2483>.

1105 Swart, N. C., and Coauthors, 2019a: CCCma CanESM5-CanOE model output prepared for CMIP6
1106 CMIP historical. Earth System Grid Federation, <https://doi.org/10.22033/ESGF/CMIP6.10260>.

1107 Swart, N. C., and Coauthors, 2019b: CCCma CanESM5 model output prepared for CMIP6 CMIP
1108 historical. Earth System Grid Federation, <https://doi.org/10.22033/ESGF/CMIP6.3610>.

1109 Tang, Y., S. Rumbold, R. Ellis, D. Kelley, J. Mulcahy, A. Sellar, J. Walton, and C. Jones, 2019:
1110 MOHC UKESM1.0-LL model output prepared for CMIP6 CMIP historical. Earth System Grid
1111 Federation, <https://doi.org/10.22033/ESGF/CMIP6.6113>.

1112 Tatebe, H., and M. Watanabe, 2018: MIROC MIROC6 model output prepared for CMIP6 CMIP
1113 historical. Earth System Grid Federation, <https://doi.org/10.22033/ESGF/CMIP6.5603>.

1114 Tietsche, S., and Coauthors, 2014: Seasonal to interannual Arctic sea ice predictability in current
1115 global climate models. *Geophysical Research Letters*, **41**, 1035–1043, <https://doi.org/10.1002/2013GL058755>.

1117 Topál, D., Q. Ding, J. Mitchell, I. Baxter, M. Herein, T. Haszpra, R. Luo, and Q. Li, 2020: An
1118 internal atmospheric process determining summertime Arctic sea ice melting in the next three
1119 decades: Lessons learned from five large ensembles and multiple CMIP5 climate simulations.
1120 *Journal of Climate*, **33**, 7431–7454, <https://doi.org/10.1175/JCLI-D-19-0803.1>.

1121 Trenberth, K. E., 1997: The Definition of El Niño. *Bulletin of the American Meteorological Society*,
1122 **78**, 2771–2778, [https://doi.org/10.1175/1520-0477\(1997\)078<2771:TDOENO>2.0.CO;2](https://doi.org/10.1175/1520-0477(1997)078<2771:TDOENO>2.0.CO;2).

1123 Trenberth, K. E., and D. J. Shea, 2006: Atlantic hurricanes and natural variability in 2005.
1124 *Geophysical Research Letters*, **33**, <https://doi.org/10.1029/2006GL026894>.

1125 Ukita, J., M. Honda, H. Nakamura, Y. Tachibana, D. J. Cavalieri, C. L. Parkinson, H. Koide,
1126 and K. Yamamoto, 2007: Northern Hemisphere sea ice variability: Lag structure and its
1127 implications. *Tellus, Series A: Dynamic Meteorology and Oceanography*, **59** (2), 261–272,
1128 <https://doi.org/10.1111/j.1600-0870.2006.00223.x>.

1129 VanAchter, G., L. Ponsoni, F. Massonnet, T. Fichefet, and V. Legat, 2020: Brief communication:
1130 Arctic sea ice thickness internal variability and its changes under historical and anthropogenic
1131 forcing. *Cryosphere*, **14**, 3479–3486, <https://doi.org/10.5194/tc-14-3479-2020>.

1132 Vance, T. R., A. S. Kiem, L. M. Jong, J. L. Roberts, C. T. Plummer, A. D. Moy, M. A. Cur-
1133 ran, and T. D. van Ommen, 2022: Pacific decadal variability over the last 2000 years and
1134 implications for climatic risk. *Communications Earth and Environment*, **3**, <https://doi.org/10.1038/s43247-022-00359-z>.

1136 Voldoire, A., 2018: CNRM-CERFACS CNRM-CM6-1 model output prepared for CMIP6 CMIP
1137 historical. Earth System Grid Federation, <https://doi.org/10.22033/ESGF/CMIP6.4066>.

1138 Volodin, E., and Coauthors, 2019: INM INM-CM5-0 model output prepared for CMIP6 CMIP
1139 historical. Earth System Grid Federation, <https://doi.org/10.22033/ESGF/CMIP6.5070>.

1140 Wang, M., and J. E. Overland, 2012: A sea ice free summer Arctic within 30 years:
1141 An update from CMIP5 models. *Geophysical Research Letters*, **39**, 6–11, <https://doi.org/10.1029/2012GL052868>.

1143 Wang, Q., S. Danilov, L. Mu, D. Sidorenko, and C. Wekerle, 2021: Lasting impact of winds
1144 on Arctic sea ice through the ocean's memory. *Cryosphere*, **15**, 4703–4725, <https://doi.org/10.5194/tc-15-4703-2021>.

1146 Watanabe, S., and Coauthors, 2021: MIROC MIROC-ES2H model output prepared for CMIP6
1147 CMIP historical. Earth System Grid Federation, <https://doi.org/10.22033/ESGF/CMIP6.5601>.

1148 Weijer, W., W. Cheng, O. A. Garuba, A. Hu, and B. T. Nadiga, 2020: CMIP6 Models Predict Sig-
1149 nificant 21st Century Decline of the Atlantic Meridional Overturning Circulation. *Geophysical
1150 Research Letters*, **47**, <https://doi.org/10.1029/2019GL086075>.

1151 Wieners, K.-H., and Coauthors, 2019: MPI-M MPIESM1.2-LR model output prepared for CMIP6
1152 historical. Earth System Grid Federation, <https://doi.org/10.22033/ESGF/CMIP6.6595>.

1153 Wu, T., and Coauthors, 2018: BCC BCC-CSM2MR model output prepared for CMIP6 CMIP
1154 historical. Earth System Grid Federation, <https://doi.org/10.22033/ESGF/CMIP6.2948>.

1155 Wyburn-Powell, C., A. Jahn, and M. England, 2022: Modeled Interannual Variability of Arctic
1156 Sea Ice Cover is Within Observational Uncertainty. *Journal of Climate*, 1–35, <https://doi.org/10.1175/jcli-d-21-0958.1>.

1158 Yeager, S. G., A. R. Karspeck, and G. Danabasoglu, 2015: Predicted slowdown in the rate of
1159 Atlantic sea ice loss. *Geophysical Research Letters*, **42**, 10 704–10 713, <https://doi.org/10.1002/2015GL065364>.

1161 Yuan, X., M. R. Kaplan, and M. A. Cane, 2018: The interconnected global climate system-
1162 a review of tropical-polar teleconnections. American Meteorological Society, 5765–5792 pp.,
1163 <https://doi.org/10.1175/JCLI-D-16-0637.1>.

1164 Yukimoto, S., and Coauthors, 2019: MRI MRI-ESM2.0 model output prepared for CMIP6 CMIP
1165 historical. Earth System Grid Federation, <https://doi.org/10.22033/ESGF/CMIP6.6842>.

1166 Zebiak, S. E., 1993: Air–sea interaction in the equatorial atlantic region. *Journal of Climate*, **6**,
1167 1567–1586, [https://doi.org/10.1175/1520-0442\(1993\)006<1567:AIITEA>2.0.CO;2](https://doi.org/10.1175/1520-0442(1993)006<1567:AIITEA>2.0.CO;2).

1168 Zhang, J., and Coauthors, 2018: BCC BCC-ESM1 model output prepared for CMIP6 CMIP
1169 historical. Earth System Grid Federation, <https://doi.org/10.22033/ESGF/CMIP6.2949>.

1170 Zhang, M., W. Perrie, and Z. Long, 2019: Springtime North Pacific Oscillation and summer
1171 sea ice in the Beaufort sea. *Climate Dynamics*, **53 (1-2)**, 671–686, <https://doi.org/10.1007/s00382-019-04627-1>.

1173 Zhang, R., and J. M. Wallace, 2015: Mechanisms for low-frequency variability of summer Arctic
1174 sea ice extent. *Proceedings of the National Academy of Sciences of the United States of America*,
1175 **112**, <https://doi.org/10.1073/pnas.1422296112>.

¹¹⁷⁶ Zhang, S., T. Y. Gan, and A. B. Bush, 2020: Variability of Arctic sea ice based on quantile
¹¹⁷⁷ regression and the teleconnection with large-scale climate patterns. *Journal of Climate*, **33** (10),
¹¹⁷⁸ 4009–4025, <https://doi.org/10.1175/JCLI-D-19-0375.1>.

¹¹⁷⁹ Ziehn, T., and Coauthors, 2019: CSIRO ACCESS-ESM1.5 model output prepared for CMIP6
¹¹⁸⁰ CMIP historical. Earth System Grid Federation, <https://doi.org/10.22033/ESGF/CMIP6.4272>.

¹¹⁸¹ Ærthun, M., I. H. Onarheim, J. Dörr, and T. Eldevik, 2021: The Seasonal and Regional Transition
¹¹⁸² to an Ice-Free Arctic. *Geophysical Research Letters*, **48**, e2020GL090825, <https://doi.org/10.1029/2020GL090825>.

Supporting Information for “Large-Scale Climate Modes Drive Low-Frequency Regional Arctic Sea Ice Variability”

Christopher Wyburn-Powell^a, Alexandra Jahn^a

⁴ ^a *Department of Atmospheric and Oceanic Sciences, and Institute of Arctic and Alpine Research,
5 University of Colorado Boulder, Boulder, Colorado*

⁶ Corresponding author: C Wyburn-Powell, chwy8767@colorado.edu

S1. Machine Learning Method Details

a. Splitting for training, validation and testing

For each LE we divide the members into training, validation, and testing sets with 75%, 15%, 10% of members respectively. For the MMLE 3+, we then use the first member for the training data set, the second member for the validation set, and leave the third and any other members for testing. For the MMLE 30+, we pool the first 23 members from all 8 GCMs for training, we use the next 4 members for validation, and the final 3 or more members for testing. As we use 74 years of data for each ensemble member (1920-2014) the smallest LE uses 74 years with 21 ensemble members, yielding an effective 1554 years for training - far in excess of observations and typically longer than pre-industrial control runs from any individual GCM. The MMLE3+ has 2294 years of training data and the MMLE 30+ maximizes the number of training years at 13,320, allowing us to determine whether substantially increasing the training data provides any gain in predictive skill.

b. Neural network configurations

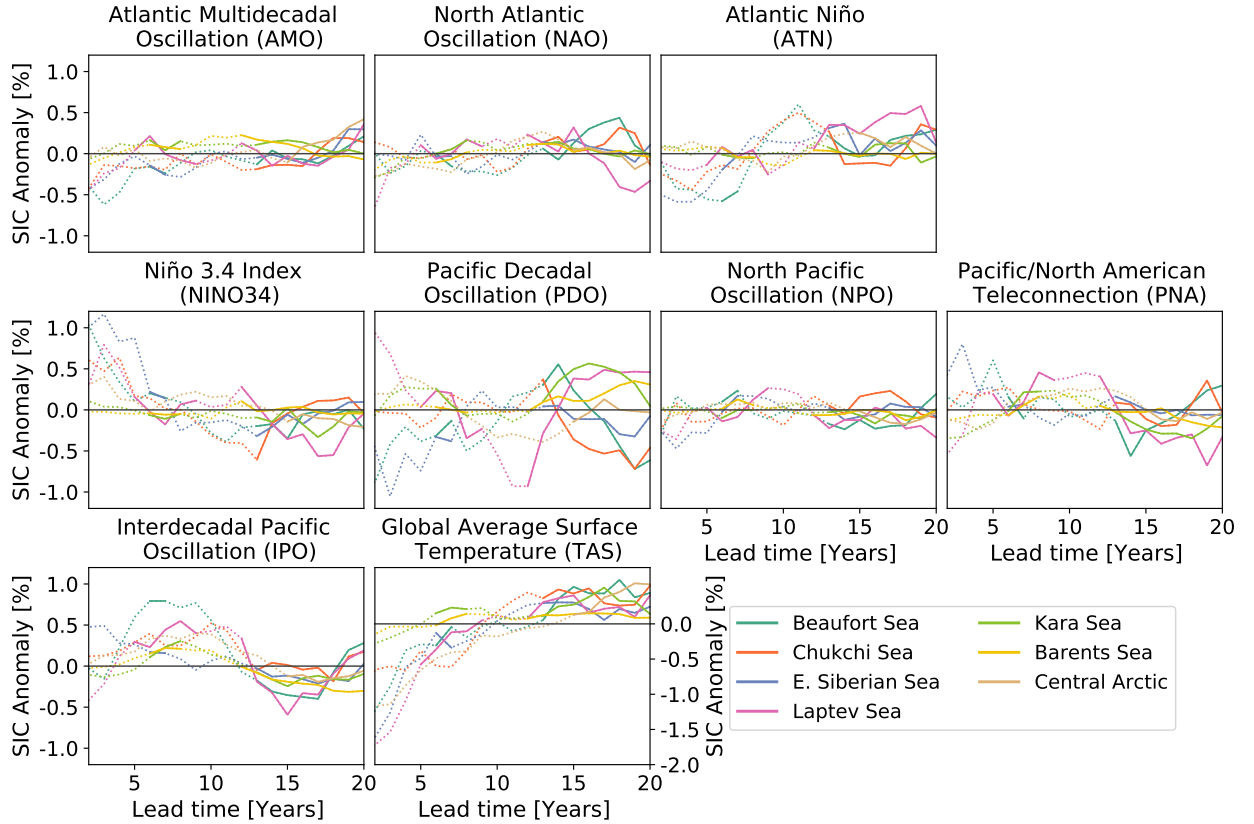
All of the four machine learning models (see section 2.2 for a physical explanation of their utility) use a fully-connected neural network with the same L1 loss function to encourage sparseness and an Adam optimizer for suitability to the four diverse models. We selected models 1 and 2 to have no bias term, which ensures the zero values of the standardized input variables (a neutral phase of the climate mode) predicts a zero SIC anomaly. With these four machine learning models, as detailed below, we can separate the effect of linear/nonlinear activation functions from the effect of additional neural network layers which allows one climate variable to interact with another:

- Model 1 - Model layers: 9-1 with linear activation functions and no bias.
- Model 2 - Model layers: 9-1 with nonlinear (ReLU) activation functions and no bias.
- Model 3 - Model layers: 9-3-3-1 with linear activation functions with bias.
- Model 4 - Model layers: 9-3-3-1 with nonlinear (ReLU) activation functions with bias.

By comparing the predictive skill of model 1 versus 2 and model 3 versus 4 we can identify the effect of increasing the model complexity from a linear to nonlinear activation functions. This is because the only difference between those two groups is the activation function, analogous to linear or nonlinear relationships between the climate modes of variability and SIC. Then, by comparing the predictive skill of models 1 versus 3 as well as model 2 versus 4, we can determine the difference in allowing the climate modes of variability to be independent of one another. This independence is facilitated in the simple models 1 and 2 where each of the 9 neurons in the input layer connects directly with the output layer. Models 3 and 4 which take into account covariance of different climate modes, this is achieved by connecting the input layer to two hidden intermediate layers of 3 fully-connected neurons before reaching the output layer.

c. Determining dominant seasons

We first compute our machine learning models on four seasonal values for each of our 9 input variables for the LE datasets and find the most dominant season averaged over all 7 regions of the Arctic for September. This is done by using model 1 with model layers of 36-1 and a linear activation function, and then selecting the largest seasonal input. We considered this reduction in seasons necessary due to the slowest changing climate modes such as the IPO having very similar seasonal values, resulting in over-fitting. Using all 4 seasons for some climate modes and a single season for one would not allow a fair comparison between climate modes, while using only one season rather than four does not substantially decrease the predictive skill. However, there is a limitation of this approach, whereby the dominant season for a given climate mode may differ between the GCMs, regions, and SIC anomaly months. Further, 'best' seasons for some climate modes of variability have little physical meaning as no season has much influence on Arctic sea ice.



7 **FIG. S1. Linear drivers of regional sea ice concentration anomalies for a reduced time period.** Same as
 8 Figure 4, except for the reduced time period of 1970-2014 instead of 1920-2014. By comparing this figure with
 9 Figure 4, we can see that the modes of variability have a similar influence as for the 1920-2014 time period,
 10 although the results are far more noisy and predictive skill does not exceed persistence for as much of the lead
 11 times as for the period 1920-2014.

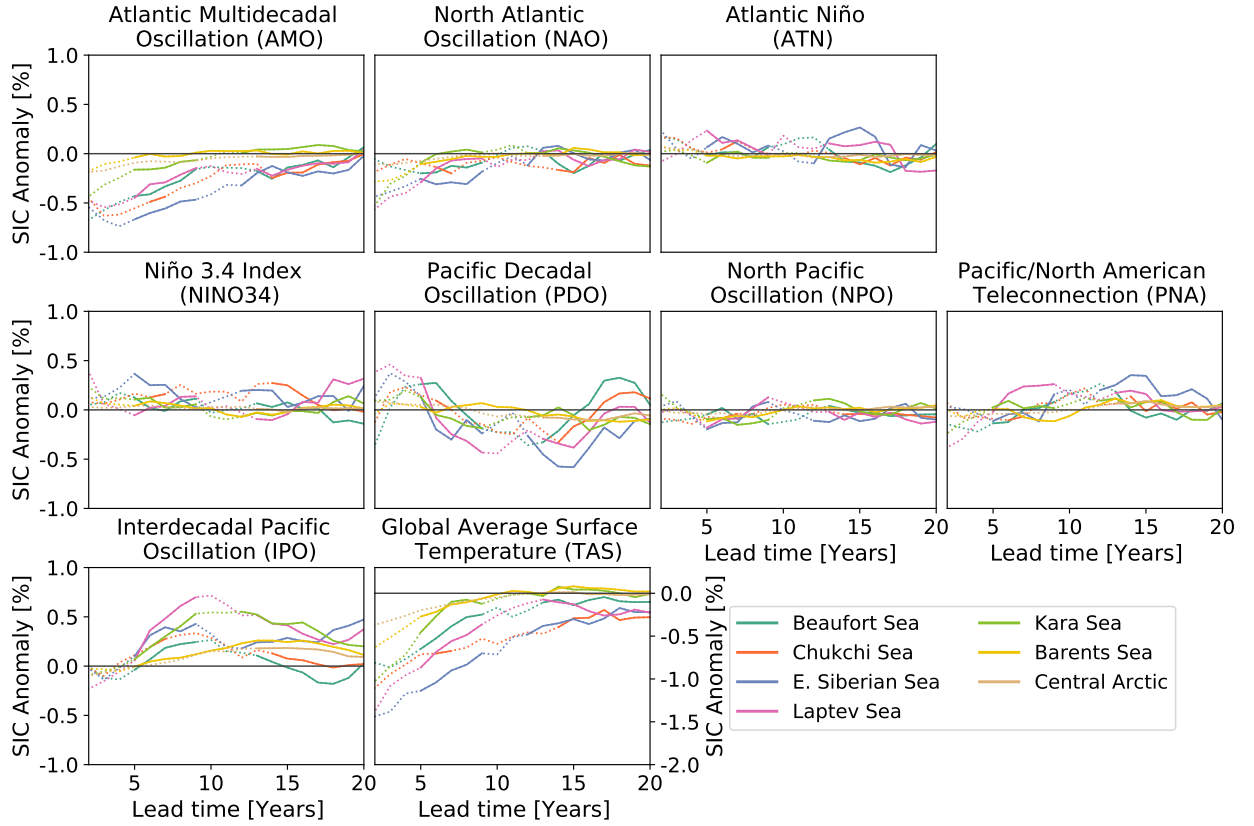
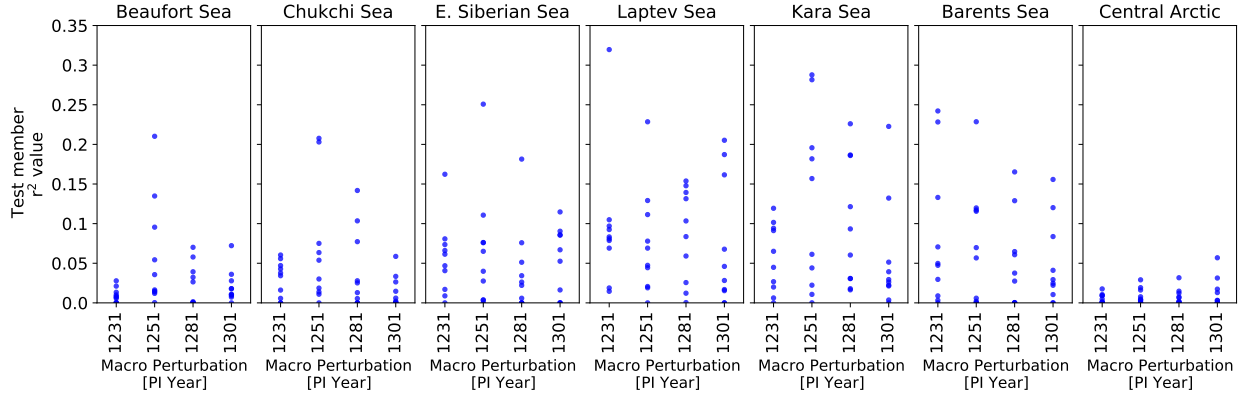
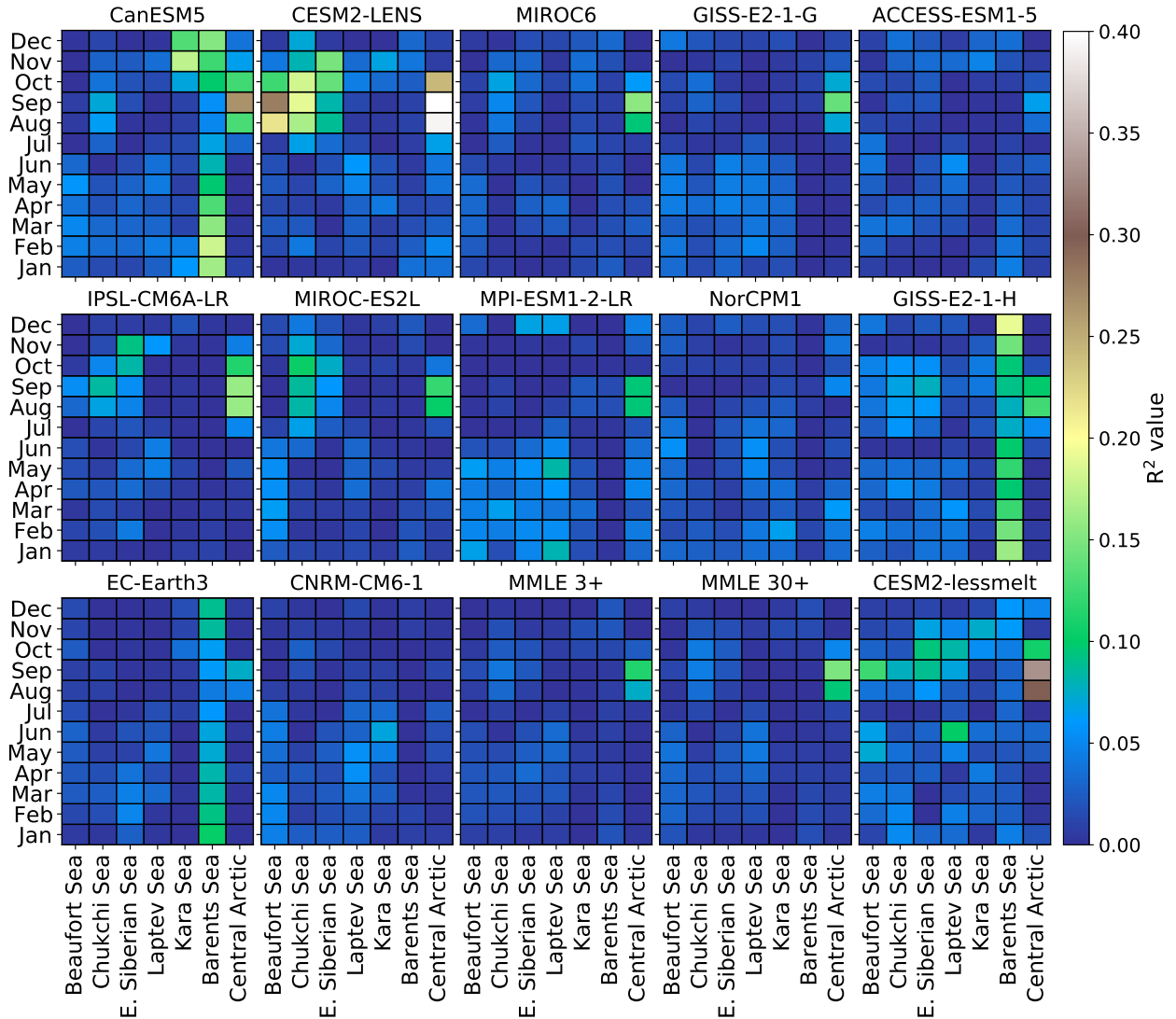


FIG. S2. Linear drivers of regional sea ice concentration anomalies for pre-industrial control runs.

Same as Figure 4 and S1, except here using the 1850 control simulations instead of the period 1920-2014 in the historical simulations. As for Figure S1, the influence of the climate variability modes are very similar as for the period 1920-2014 (Figure 4), but the coefficients are smaller, likely due to the lower variability in the pre-industrial mean state. Instead of different ensemble members, the available 35 GCMs are each split into several members of 74 year length each, with the first 222 years used for training and the following 74 years for validation.



19 **FIG. S3. Influence of macro versus micro initializations in the CESM2-LENS on September test member**
 20 **r^2 values.** Of the 48 test members from the CESM2-LENS (see Figure 6), 12 are created through macro
 21 initializations by choosing different start years from the pre-industrial simulation, and hence differ in their ocean
 22 and atmospheric state. Of those 12, four (here shown on the x-axis by branch year) have 9 additional ensemble
 23 members branched from them, which all only differ slightly in their atmospheric state due to small atmospheric
 24 perturbations, i.e., referred to as micro initializations. Here we show these latter 40 simulations (blue circles),
 25 to assess whether macro or micro initializations dominate the possible r^2 values (with persistence removed). As
 26 the four distributions of 10 realizations for each macro initialization are very similar, this shows that the ocean
 27 state (macro perturbation) can influence the predictive skill, but generally does not narrow the potential range of
 28 r^2 values which can occur due to micro perturbation.



29 FIG. S4. Persistence r^2 values for LEs, MMLEs, and CESM2-lessmelt at a 5-year lag time. This figure
 30 shows the persistence r^2 value that was subtracted from the absolute value of the validation r^2 in Figure 3.
 31 Additionally the CESM2-lessmelt persistence is shown for comparison with CESM2-LENS. CESM2-lessmelt
 32 has a thicker sea ice mean state than CESM2-LENS and, as shown in this figure, has a smaller persistence
 33 validation r^2 value, although this value is still an outlier compared with the other GCMs.